1. Galaxy Observations

1.1. Overview and General Comments

Many studies for many types of galaxies at various redshifts have demonstrated that there is a correlation between the galaxy luminosity and the mean metallicity of a galaxy. By galaxy luminosity we mean emitted flux across a wavelength bandpass sufficiently red that current star formation has little impact, and that the light there is dominated by that from the accumulation of previous generations of stars. Thus, for example, a rest frame blue or UV luminosity is not ideal, as luminous young stars make a big contribution there. The conversion of luminosity to mass, to make this a mass – metallicity relation, is much more straightforward for redder colors, but not so red that dust emission dominates over thermal emission from stars.

There have been a number of explanations proposed to explain the $M - Z$ relation. Among them is that a galaxy wide wind transporting metal-enriched ISM gas from the galaxy to the IGM is much less effective in more massive galaxies. In low mass galaxies, with lower binding energies, it is much easier to sustain a galactic outflow, thus losing a large fraction of the metal porduction injected into the ISM from stars. Furthermore many luminous galaxies have high gass mass fractions. Recall the solution to the simple closed box model, namely Z is function of the gass mass fraction (and the nucleosynthetic yields), with lower gass mass fraction corresponding to higher metallicity.

Another factor important to galaxy evolution is the growth and feedback from a central AGN. The existence of luminous QSOs at high redshift means AGN develop very quickly after a galaxy forms. AGN feedback on the ISM, especially in the galaxy central region, may be important in setting the maximum mass of galaxies.

1.2. Nearby Galaxies as revealed by the SDSS

The impact of the SDSS in this field has been profound. The combination of huge samples observed and processed in a uniform manner, an easily searchable database with intermittant public releases of hundreds of thousands of spectra, and precision 5 color photometry, has been revolutionary. The SDSS magnitude limit means that galaxies with redshifts beyond $z \sim 0.3$ are difficult to reach, but out to that distance, the SDSS changed the nature of the field.

The major concern in studies based on SDSS spectra is the fixed fiber size of 3 arcsec, which means aperture corrections are important as the spatial sampling varies from "nuclear spectra" to "partial or full disk spectra" depending on the redshift. Given radial gradients in metallicity (and in many other galaxy variables), such corrections must be evaluated.

Initial work on large samples of nearby galaxies focused first on star-forming galaxies. The presence of strong emission lines in their spectra meant large samples reaching to larger distances were more easily achieved than for galaxies with only absorption lines. The first papers established methods for measuring galaxy masses and determining their SFR from the SDSS spectra. Kaufmann et al (2003a,b) use the 4000 Å break (arising from old stars) combined with the Balmer absorption in Hδ (from hotter stars) to determine crudely the mean stellar ages of galaxies and the fractional stellar mass formed in bursts over the past few Gyr. The latter is determined crudely from the line emission in Hδ divided by the continuum emission near that wavelength, combined with model galaxy predictions.

This, combined with multi-color broad band photometry, then yields estimates of the dust absorption within the galaxy and of the stellar mass. The mass-to-light ratio then follows. Even if the uncertainties are substantial (they quote a 95% confidence level of 40% uncertainties in galaxy stellar mass), with more than 100,000 SDSS spectra of galaxies, trends become much more clear than with much smaller older datasets. Their data analysis

uses Bayesian likelihood estimates for some parameters. Key conclusions from these papers are that most of the stellar mass in galaxies resides in those with masses within a factor of two of $\sim 5 \times 10^{10}\ M_{\odot}$, and they find the distribution of the amplitude of the 4000 Å break is bimodal, suggesting a clear division between old and "dead" galaxies and galaxies with more recent star formation.

Their second paper (Kaufmann, Heckman & White et al, 2003, MNRAS, 341, 54) proceeds to use the above characterizations to study the relations between stellar mass, star formation history, size, and internal structure (concentration of light and surface mass density) in low redshift SDSS galaxies. Many of these trends (for example, that lower mass galaxies have younger stellar populations, low surface brightness, and low concentrations typical of disks) had been known to exist for some time, but the sheer number of SDSS galaxy spectra makes them much clearer.

The conclusions they derive are that low mass galaxies form with little angular momentum loss through cooling and condensation within a gravitationally dominant dark matter halo. Their stellar mass empirically is found to be proportional to $M(halo)^{3/2}$. They suggest that the efficiency of conversion of baryons into stars in low mass galaxies is proportional to the halo mass, perhaps due to SN feedback. Galaxies with old stellar populations, high surface mass densities, and bulges are concentrated among the most massive ones with $M > 3 \times 10^{10}\ M_{\odot}$. The star formation efficiency decreases for the highest mass halos, and once massive galaxies are assembled, little star formation occurs.

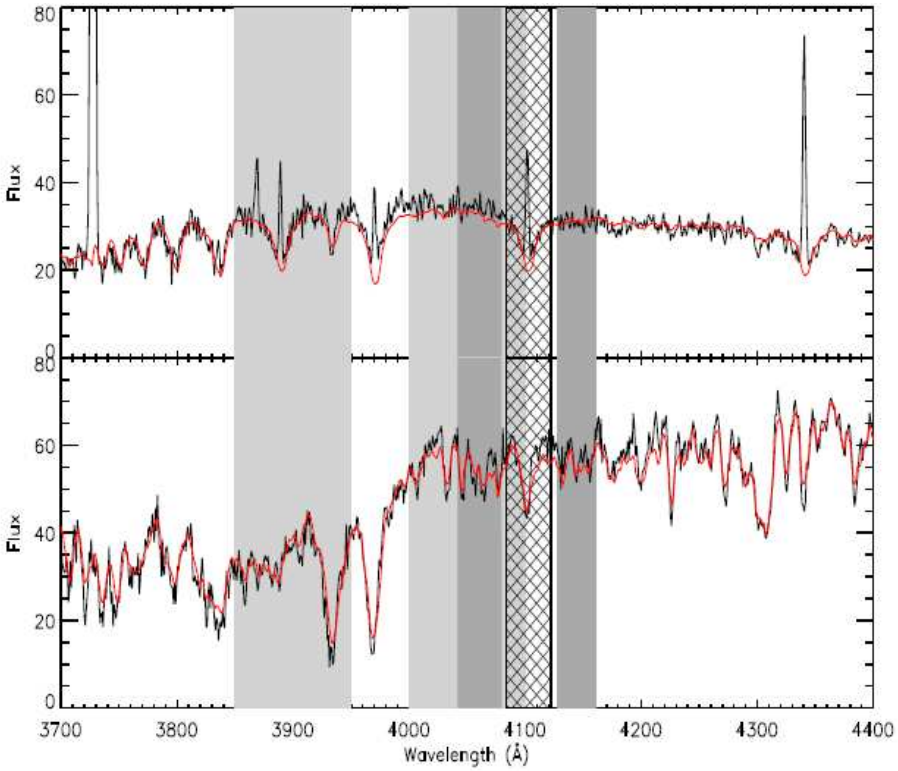

Figure 1: SDSS spectra of a late-type galaxy (top) and an early-type galaxy (bottom) are plotted over the interval 3700-4400 Å in the restframe. The red line shows our best fit BC2002 model spectrum. The light grey shaded regions indicate the bandpasses over which the $D_n(4000)$ index is measured. The dark grey regions show the pseudocontinua for the $H\delta_A$ index, while the hatched region shows the $H\delta_A$ bandpass.

Fig. 1.— Fig. 1 of Kauffmann, Heckman & White et al, 2003, MNRAS, 341, 33.

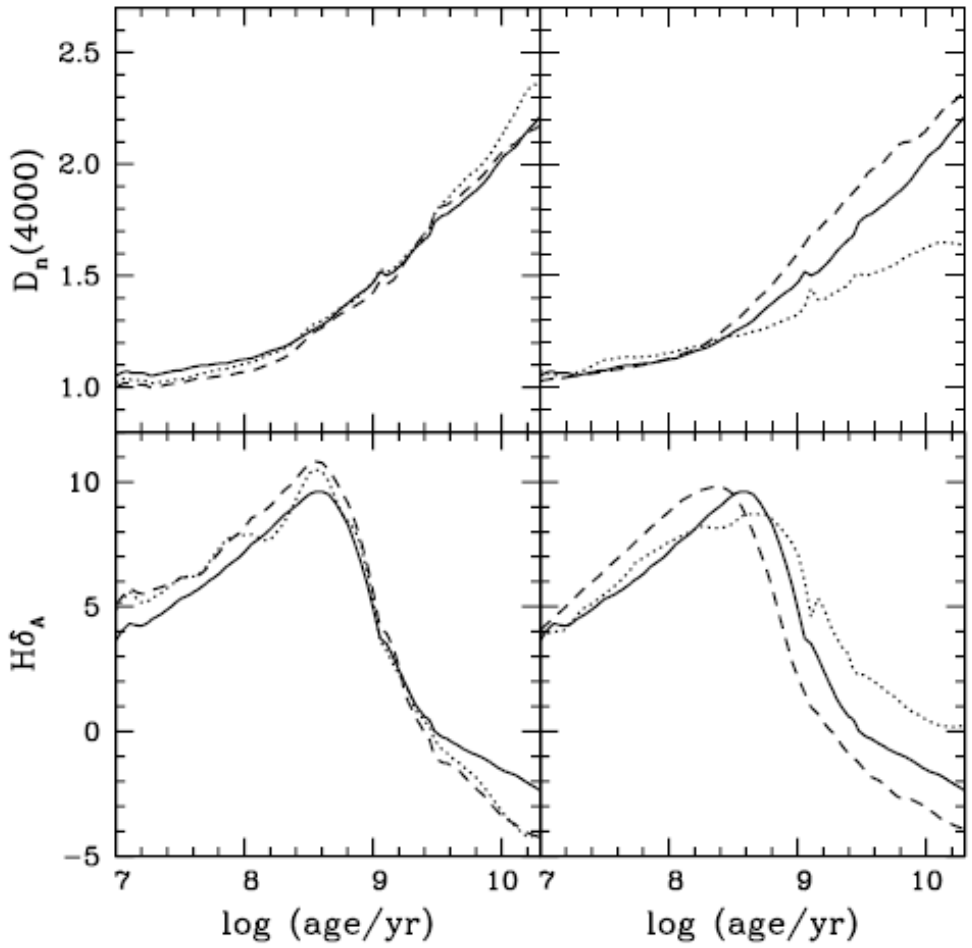

Figure 2: **Left:** The evolution of $D_n(4000)$ and $H\delta_A$ following an instantaneous, solar-metallicity burst of star formation. Solid lines show results from BC2002+STELIB, the dotted line shows results if the Pickles (1998) library is used, and the dashed line is for the Jacoby, Hunter & Christensen (1984) library. **Right:** The evolution of $D_n(4000)$ and $H\delta_A$ for bursts of different metallicity. The solid line is a solar metallicity model, the dotted line is a 20 percent solar model and the dashed line as a 2.5 solar model.

Fig. 2.— Fig. 2 of Kauffmann, Heckman & White et al, 2003, MNRAS, 341, 33.

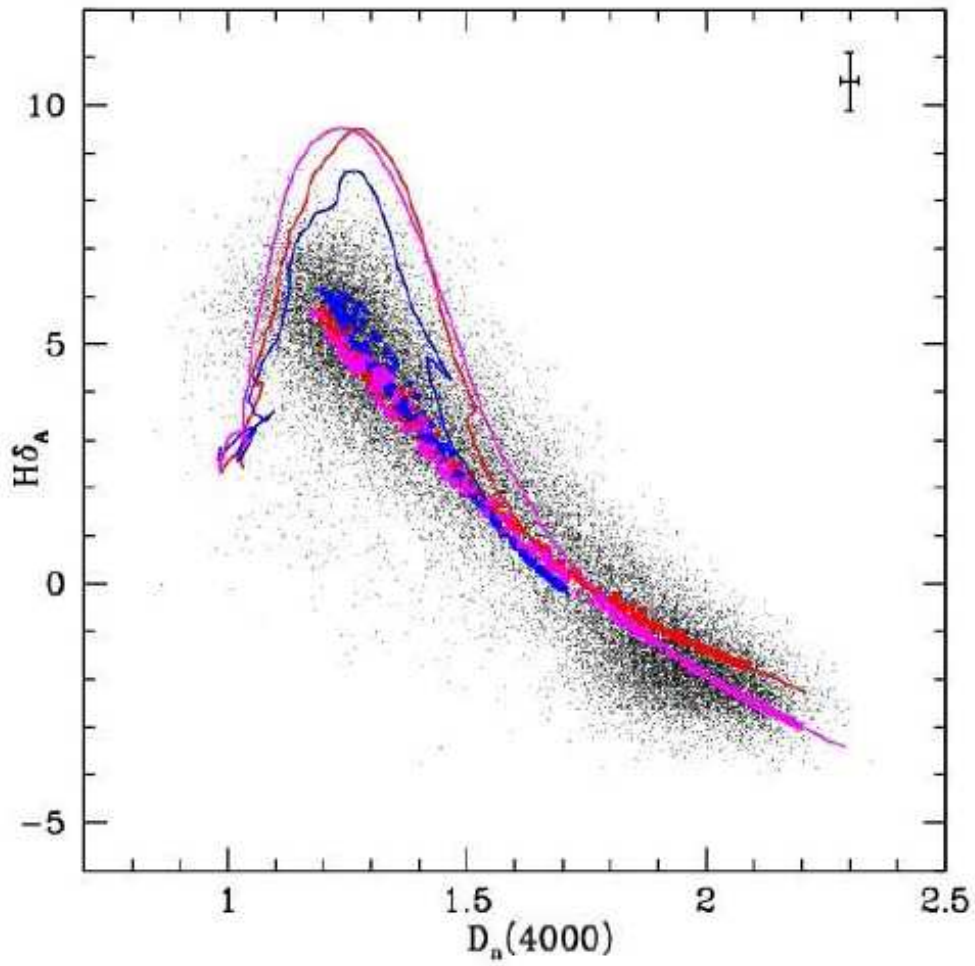

Figure 3: $H\delta_A$ is plotted as a function of $D_n(4000)$ for 20% solar, solar and 2.5 times solar metallicity bursts (blue, red and magenta lines), and for 20% solar, solar and 2.5 solar continuous star formation histories (blue, red and magenta symbols). A subset of the SDSS data points with small errors are plotted as black dots. The typical error bar on the observed indices is shown in the top right-hand corner of the plot.

Fig. 3.— Fig. 3 of Kauffmann, Heckman & White et al, 2003, MNRAS, 341, 33.

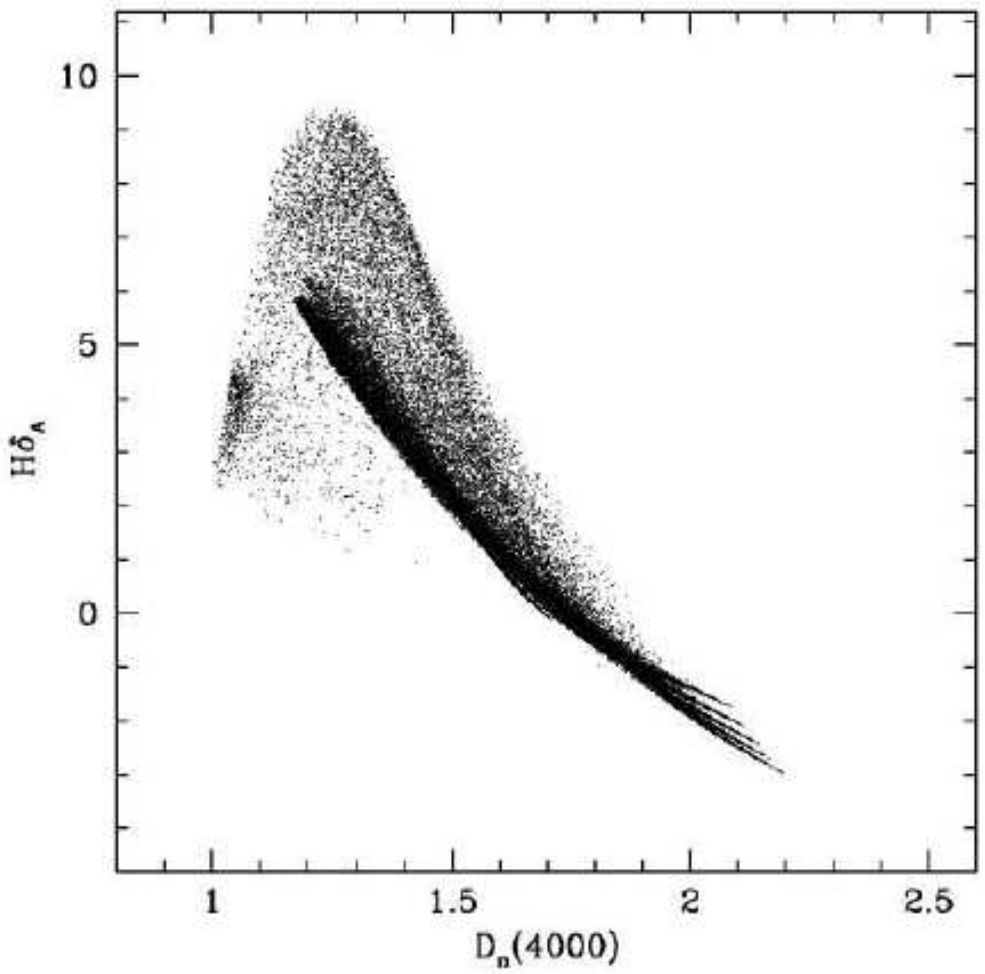

Figure 4: The distribution of galaxies in our model library in the $D_n(4000)/H\delta_A$ plane.

Fig. 4.— Fig. 4 of Kauffmann, Heckman & White et al, 2003, MNRAS, 341, 33.

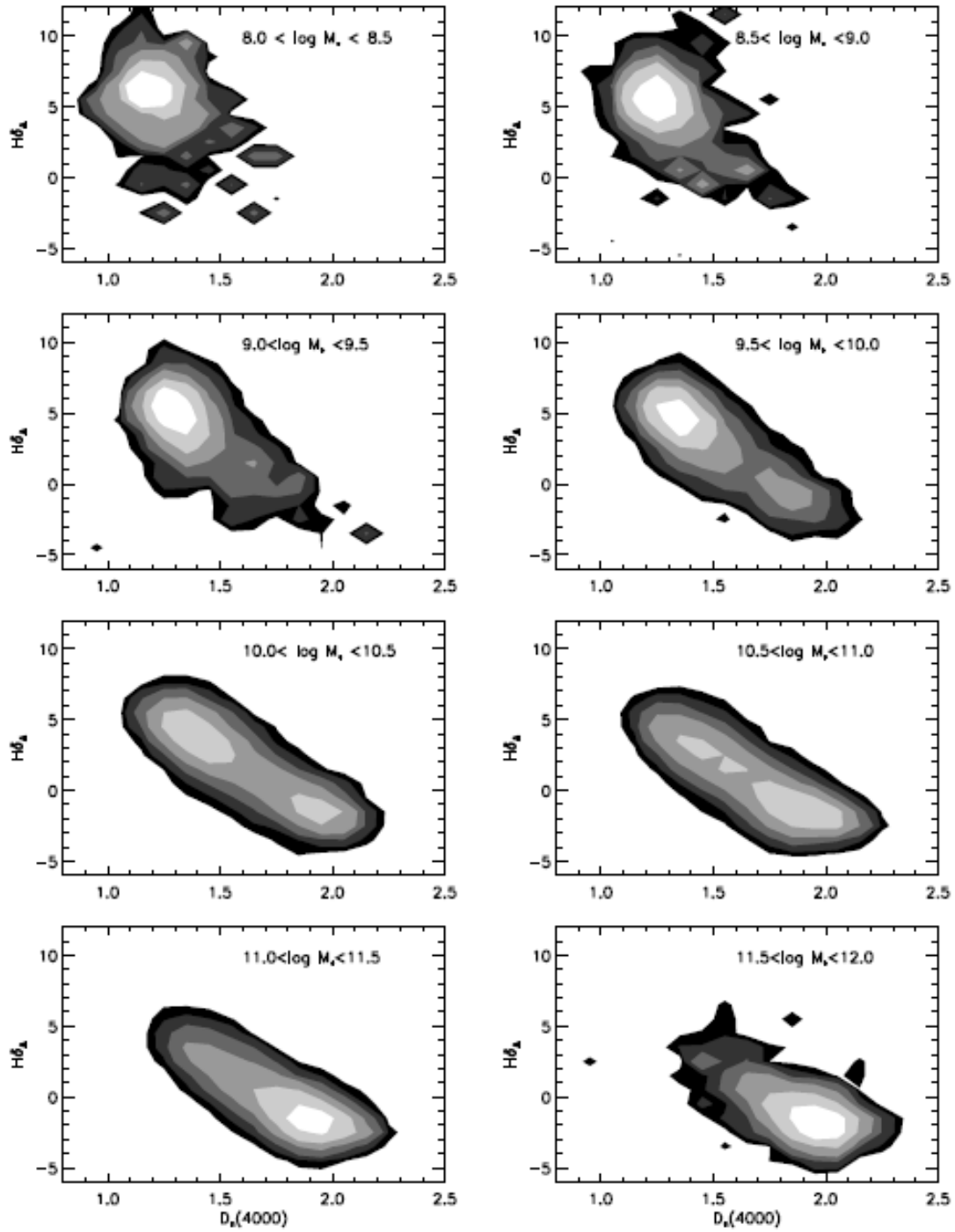

Fig. 5.— The distribution function of Hδ and $D_n(4000\text{Å})$ in 8 ranges of stellar mass. (Fig. 3 of Kauffmann, Heckman & White et al, 2003, MNRAS, 341, 54)

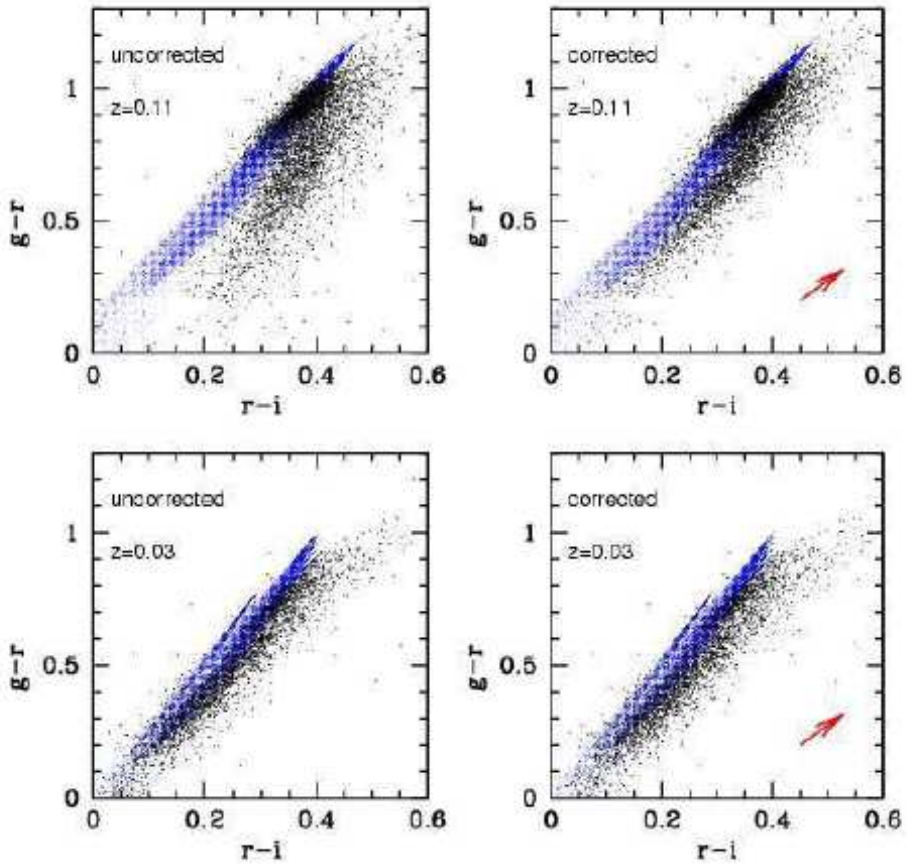

Figure 10: The observed $g - r$ versus $r - i$ spectral colours of a representative subset of SDSS galaxies (black points) are compared with our Bruzual-Charlot model grid (blue points) at $z = 0.03$ and $z = 0.11$. The colours have been computed by convolving the spectra with the SDSS filter functions. In the right panels, the colours are computed after emission lines have been removed from the spectra. The predicted reddening vector assuming an attenuation law of the form $\tau_\lambda \propto \lambda^{-0.7}$ is shown as a red arrow.

Fig. 6.— Fig. 10 of Kauffmann, Heckman & White et al, 2003, MNRAS, 341, 33.

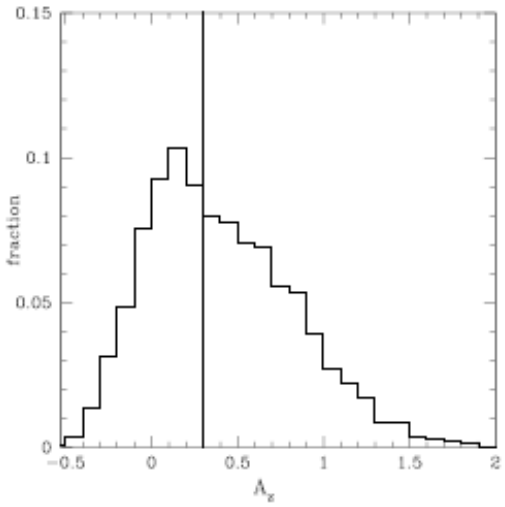

Figure 11: The distribution of the estimated values of the dust attenuation in the z-band for all the galaxies in the sample. The median value is shown as a vertical line.

Fig. 7.— Fig. 11 of Kauffmann, Heckman & White et al, 2003, MNRAS, 341, 33.

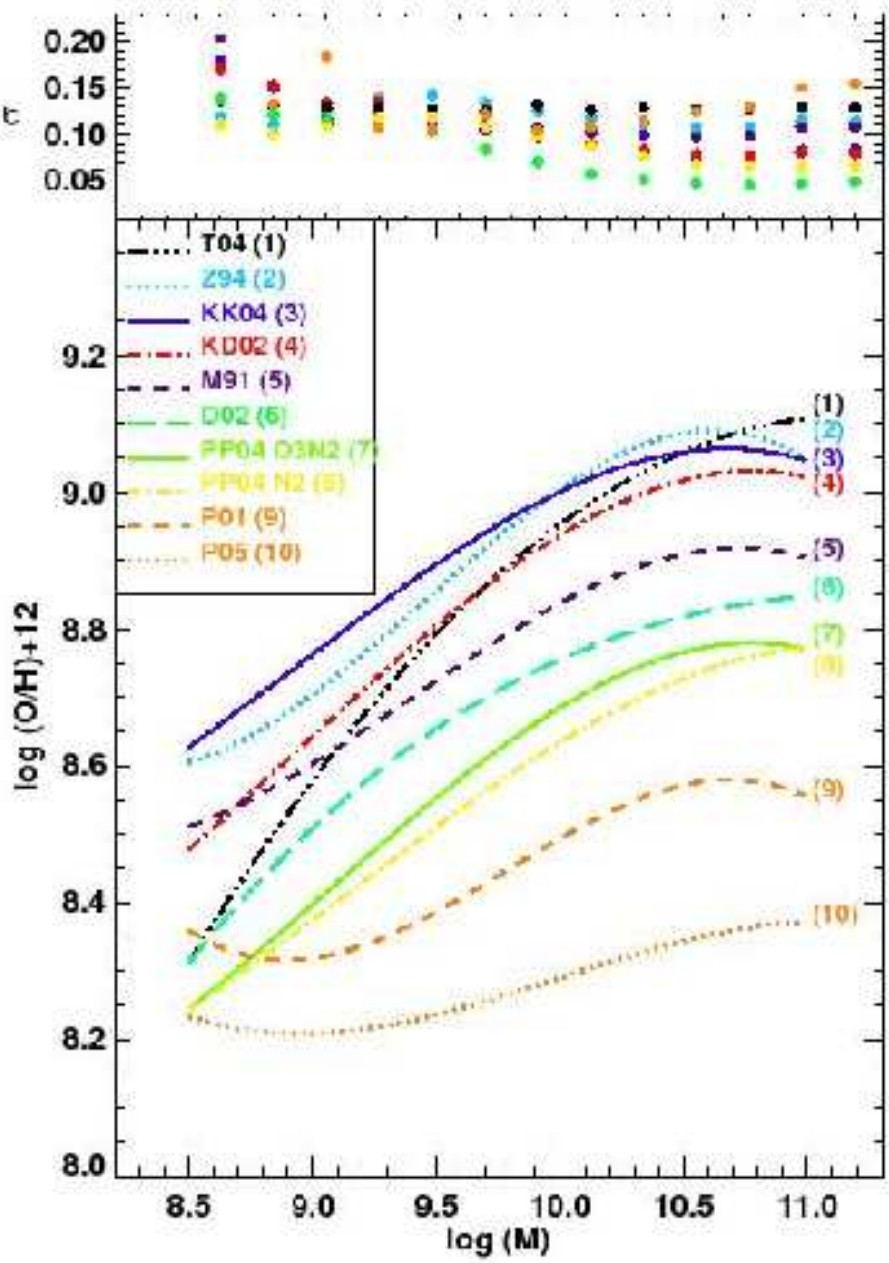

FIG. 2.— The robust best-fit mass-metallicity relations calculated using the different metallicity calibrations listed in Table 1, except the T_e-method. The top panel shows the rms scatter in metallicity about the best-fit relation for each calibration in 0.1 dex bins of stellar mass. The y-axis offset, shape, and scatter of the MZ relation differs substantially, depending on which metallicity calibration is used.

Fig. 8.— Fig. 2 of Kewley & Ellison (2008, ApJ, 681, 1183). These are mean relations from analyzing emission line strengths for strong lines (i.e. R_{23}) for 27,730 star-forming galaxies from the SDSS.

Tremonti, Heckman, Kauffmann et al (2004, ApJ, 613, 898) establish that there is a tight correlation between galaxy stellar mass and metallicity (i.e. oxygen abundance as determined from emission lines). This could be due to less effecient loss of SN ejecta in massive galaxies by galactic winds or to a higher speciic star formation rate in more massive galaxies. Analysis of large SDSS sample by Tremonti et al (2004) suggests galaxies do **not** evolve as closed boxes. The total baryonic mass and effective yield are correlated, with the yield increasing by a factor of 10 from low mass star-forming galaxies to the most massive star-forming galaxies; this correlation flattens out at $\sim M^{9.5}\ M_{\odot}$. They derive a fit to the observations assuming retention of SN ejecta is proportional to the depth of the potential well, which scales as V_c^2, where V_C is the galaxy circular velocity, but asymptotically approaches 100% for the most massive galaxies. (Note that $M_{\rm baryon} \propto V_C^{3.5}$). Tremonti et al develop a model for the retained fraction in terms of V_C and a single constant (V_0), which in turn yields the effective yield Y_{eff} in terms of V_C, V_0, and the yield y_0 if no metals are lost.

This study concludes that galaxy mass loss via winds is much more effective in galaxies with shallow potential wells. This is not a new idea, but the massive SDSS database allows a very clean determination of the effect.

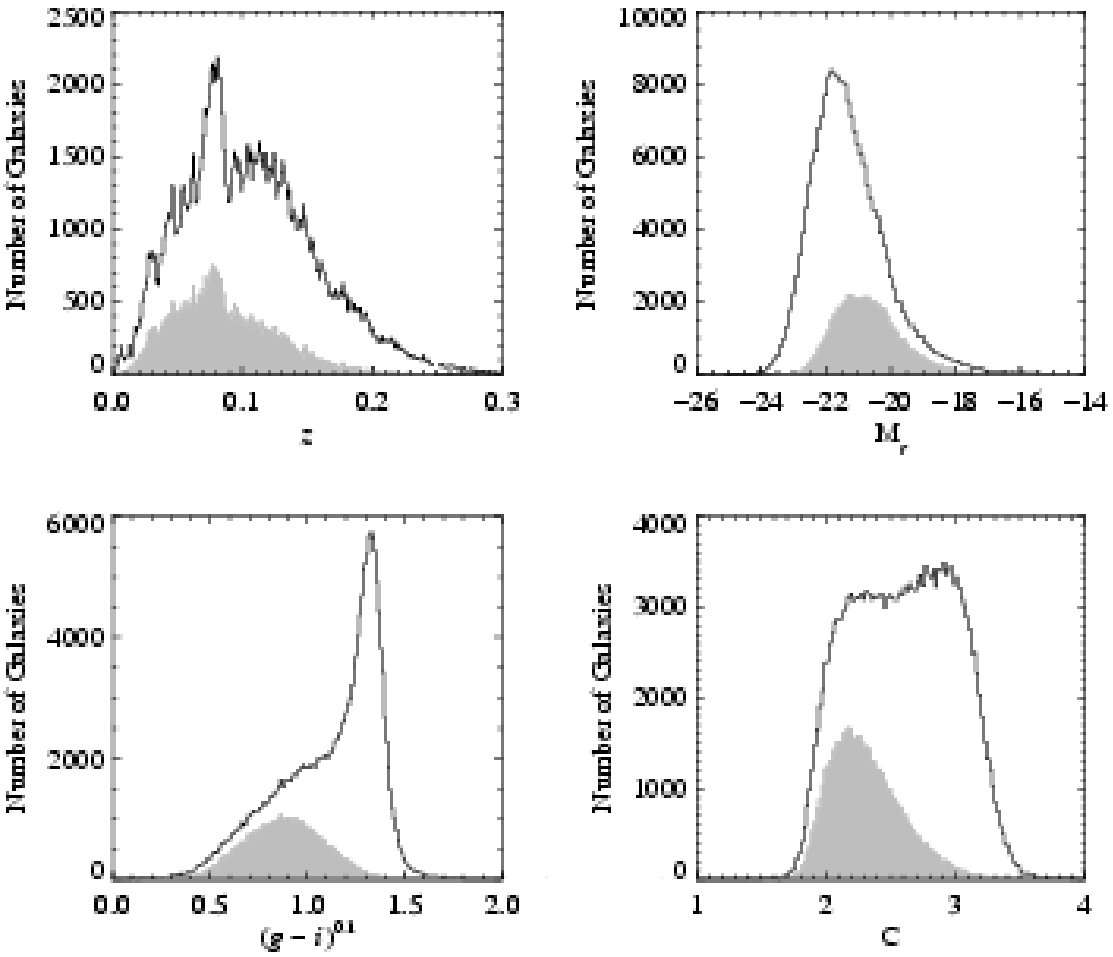

FIG. 2.— Properties of the SDSS main sample and our star-forming galaxy sample (gray shaded histograms). The upper left panel shows the redshift distribution. The upper right panel shows absolute r-band Petrosian magnitudes. The lower left panel shows the distribution of galaxy $(g-i)$ color. The colors have been k-corrected to $z = 0.1$ following Blanton et al. (2003b). The lower right panel shows the concentration index, $C = R_{90}/R_{50}$. Concentration correlates loosely with Hubble type, with $C \sim 2.6$ marking the boundary between early- and late-types.

Fig. 9.— Fig. 2 of Tremonti, Heckman, Kauffmann et al (2004, ApJ, 613, 898).

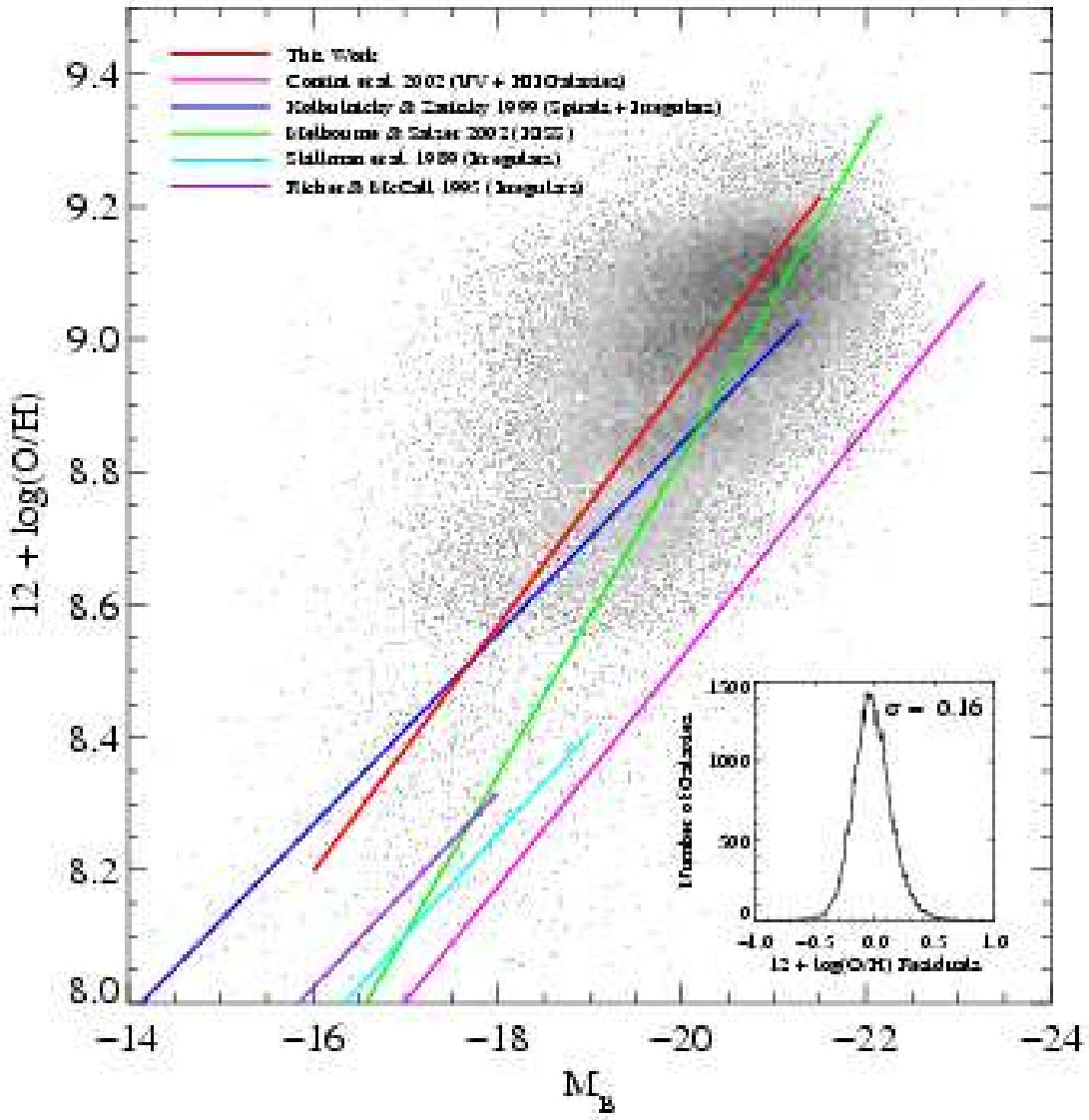

FIG. 4.— The luminocity–metallicity relation for SDSS galaxies and various galaxy samples drawn from the literature (see legend). All of the B magnitudes have been corrected to $H_0 = 70$ km s^{-1} Mpc^{-1}, but we have made no attempt to homogenize the metallicity measurements. The red line represents the linear least squares bisector fit to the SDSS data. The inset plot shows the residuals of the fit.

Fig. 10.— Fig. 4 of Tremonti, Heckman, Kauffmann et al (2004, ApJ, 613, 898).

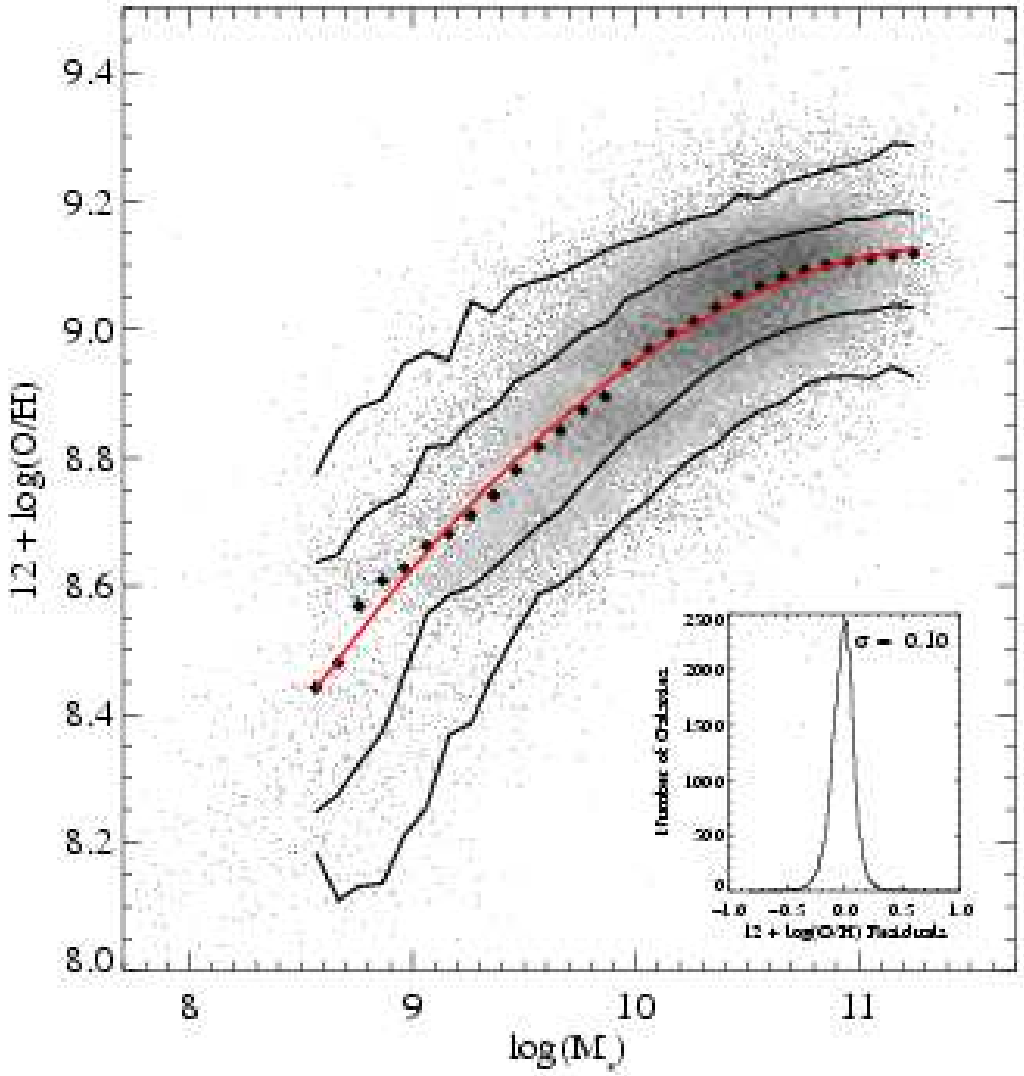

FIG. 6.— The relation between stellar mass, in units of solar masses, and gas-phase oxygen abundance for ∼53,400 star-forming galaxies in the SDSS. The large black points represent the median in bins of 0.1 dex in mass which include at least 100 data points. The solid lines are the contours which enclose 68% and 95% of the data. The red line shows a polynomial fit to the data. The inset plot shows the residuals of the fit. Data for the contours are given in Table 3.

Fig. 11.— Fig. 6 of Tremonti, Heckman, Kauffmann et al (2004, ApJ, 613, 898).

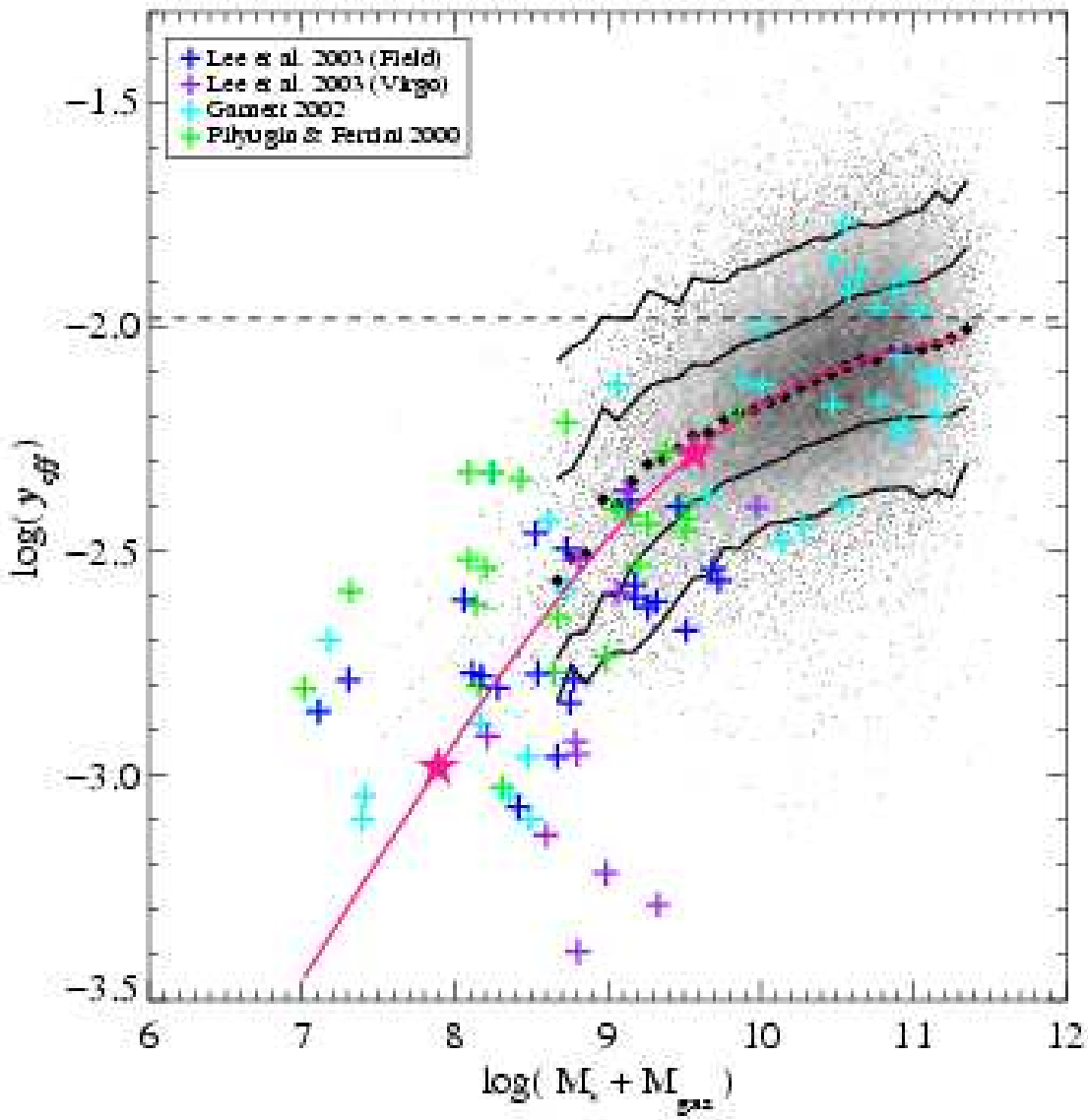

FIG. 8.— Effective yield as a function of total baryonic mass (stellar + gas mass) for 53,400 star-forming galaxies in the SDSS. The large black points represent the median of the SDSS data in bins of 0.1 dex in mass which include at least 100 data points. The solid lines are the contours which enclose 68% and 95% of the data. The colored crosses are data from Lee, McCall, & Richer 2003, Garnett 2002, and Pilyugin & Ferrini 2000. Both the metallicities and the gas masses used to derive the effective yield have been computed differently in the SDSS data and the samples from the literature. The agreement nevertheless appears quite good. The pink line is the best fit to the combined dataset assuming the intrinsic functional from given by Equation 6. The dashed line indicates y_0, the true yield if no metals are lost, derived from the fit to the data. The pink stars denote galaxies which have lost 50% and 90% of their metals. Data for the contours are given in Table 4.

1.3. Metallicity - Luminosity at intermediate redshift

A number of ground-based projects (CFGRS and Deep at Keck, VIMOS at the VLT) reach out to $z \sim 1.2$ for star-forming galaxies, after which the key emission lines for the R_{23} method are shifted into beyond 1 μm, where the detectors are noisier and the thermal and sky backgrounds larger. Kobulnicky & Kewley, 2004, ApJ, 617, 240 use the large collection of redshifts and spectra available for galaxies in the Hubble Deep Fields from Keck. They use standard R_{23} techniques to obtain the metallicities of star-forming field galaxies at $0.26 < z < 0.82$, and study the evolution of the luminosity-metallicity relation.

In this redshift range, the massive "old" galaxies are replaced by luminous star-forming galaxies. Among the star-forming galaxies, the $L - Z$ relation is clearly detected. For galaxies of similar luminosity with $z \sim 0.7$ the metallicity is 40% lower than for local galaxies of comparable luminosity, with the offset bigger at the low luminosity end and quite small at the high luminosity end of the sample. The star formation rate is larger by a factor of 7 to 10 in the mean at $z \sim 1$ than it is in the local universe. The rate of metal enrichment means that roughly 1/3 of metals in local galaxies have been synthesized since $z \sim 1$. This suggests that low-mass galaxies have lower y_{eff} than do higher-mass galaxies, or they assemble on longer timescales, or they began assembly later. Losses of up to 50% of the O produced by SN in a galaxy are necessary to avoid over-enriching the galaxies at the redshift range observed.

Beyond $z \sim 1.2$ it is necessary to either move into the near-IR or use UV features. Steidel, Shapley, Pettini et al (2004, ApJ, 592, 728) managed to reach suitable features there for star-forming galaxies with $1.4 < z < 2.5$ taking advantage of a new capability at Keck, the high blue/UV sensitivity of LRIS-B. Again galaxies are found to be metal-rich.

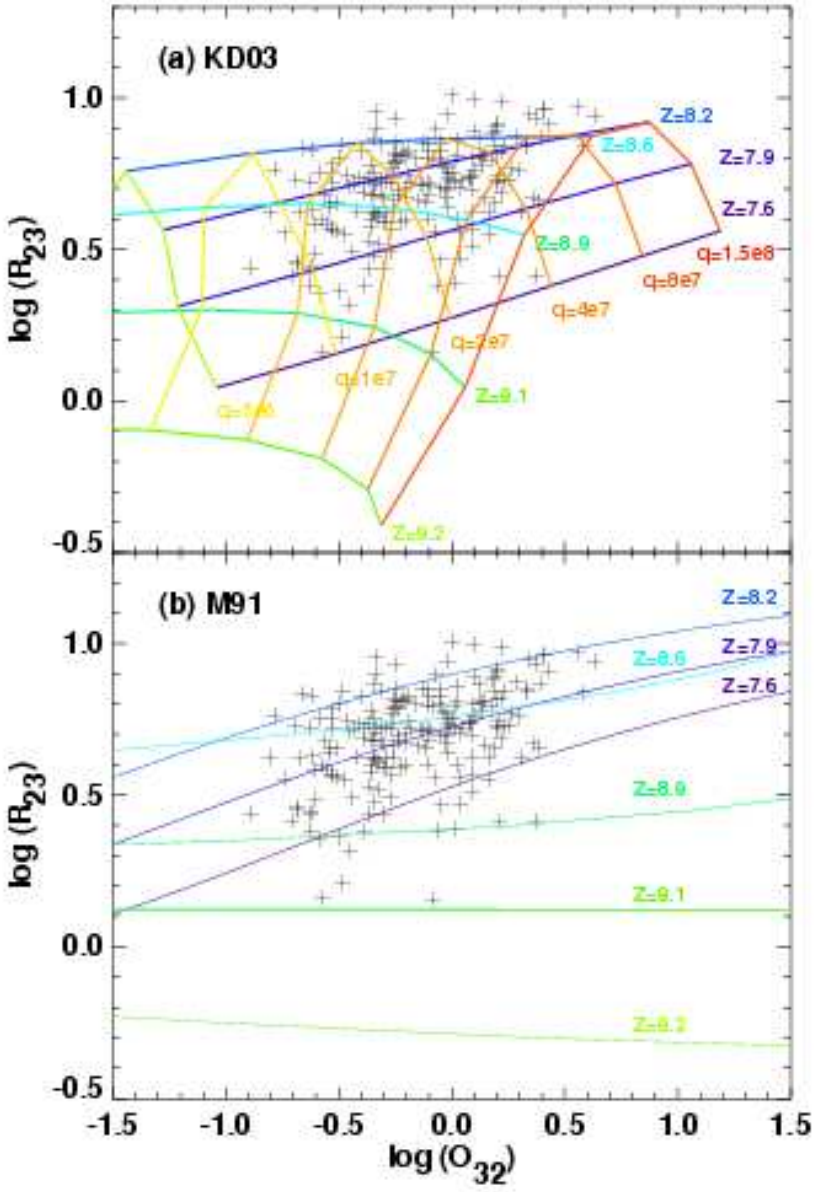

Fig. 3.— The logarithm of the metallicity-sensitive line ratio R_{23} versus the logarithm of the ionization-parameter sensitive ratio O_{32} for the TKRS galaxies. The colored curves represent the theoretical photoionization models of (a) Kewley & Dopita (2003) and (b) McGaugh (1991). Models are shown for metallicities between $12 + \log(\mathrm{O/H}) = 7.6$ (violet) to $12 + \log(O/H) = 9.1$ (green). For reference, solar metallicity is $12 + \log(\mathrm{O/H}) \sim 8.7$ (Allende Prieto *et al.* 2001). The Kewley & Dopita (2003) models for ionization parameters between $q = 5 \times 10^6 - 1.5 \times 10^8$ cm/s are shown (yellow-red curves). The TKRS data span ionization parameters $q = 1 \times 10^7 - 8 \times 10^7$ cm/s.

Fig. 13.— Fig. 3 of Kobulnicky & Kewley (2004, ApJ, 617, 240).

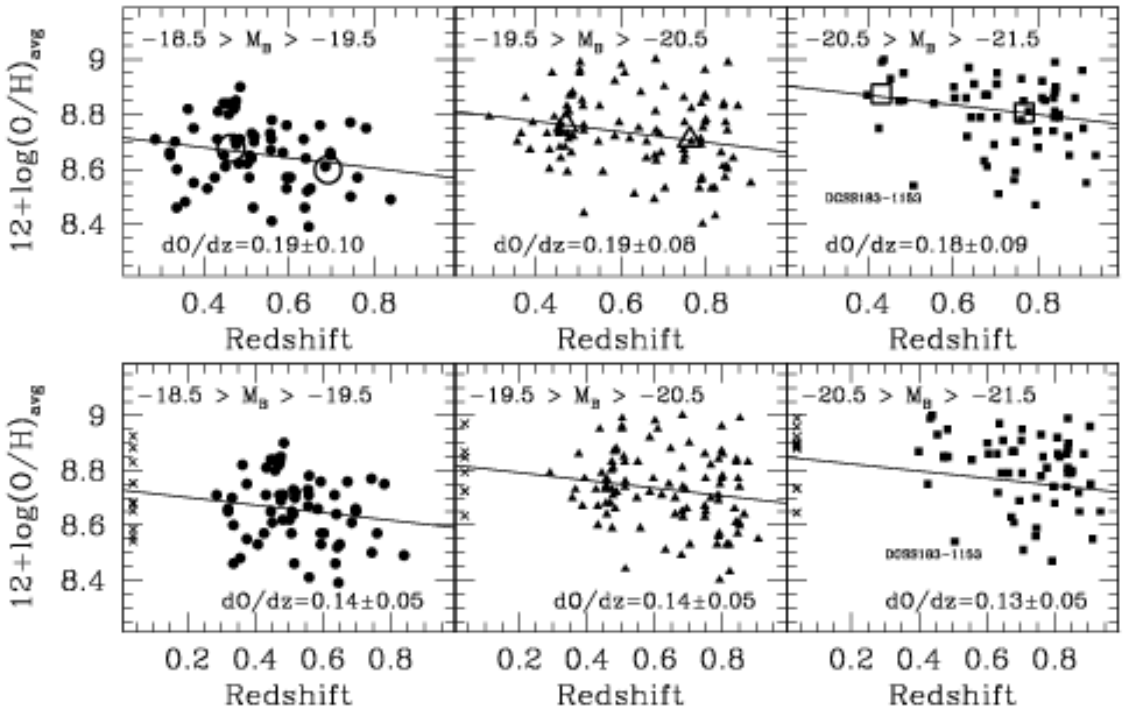

Fig. 12.— Relation between redshift and oxygen abundance for TKRS plus CFRS (LCS03) and DGSS (Ke03) galaxies in three different luminosity ranges. The upper row shows only distant galaxies. Large open symbols indicate mean values in two redshift bins: $z < 0.6$ and $z > 0.6$. The lower row shows the same data with a sample of local $z = 0$ galaxies from Jansen *et al.* (2001) and Kennicutt (1992) as defined by Ke03. The slopes of least squares fits are given in each panel. The evolution of mean oxygen abundance with redshift is ~ 0.19 dex/z in the upper row and is consistent across redshift bins. When local galaxies are considered, the slopes of the metallicity-redshift relations in all bins drop to $\sim 0.14 \pm 0.05$ dex/z.

Fig. 14.— Fig. 12 of Kobulnicky & Kewley (2004, ApJ, 617, 240).

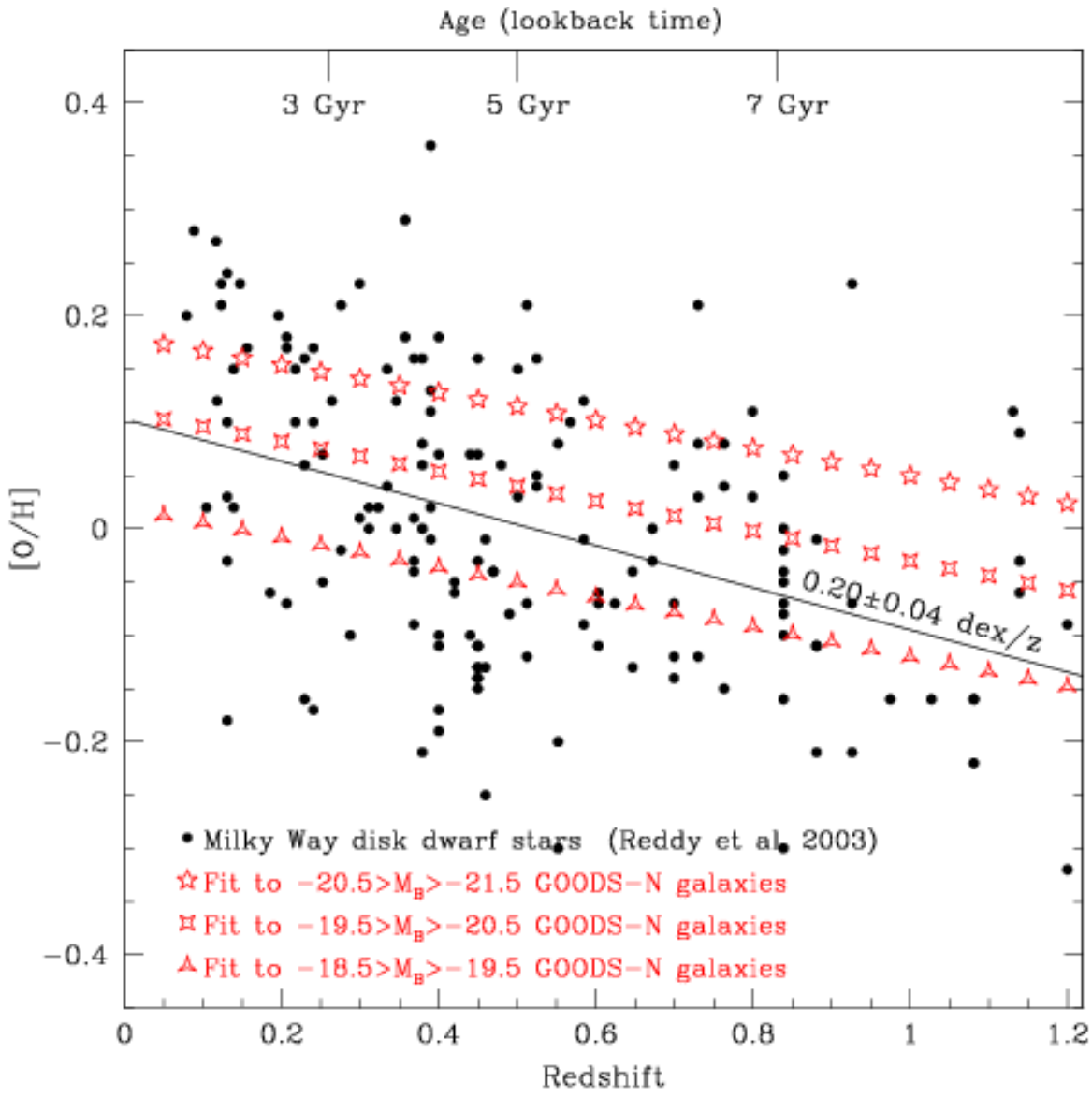

Fig. 13.— Relation between age (a.k.a lookback time) and oxygen abundance, relative to solar, for Milky Way disk stars from Reddy *et al.* (2003). The ages of the stars are plotted in terms of their equivalent redshifts (using the adopted cosmology) for direct comparison to Figure 12. The line shows a least squares linear fit to the Galactic data. The tracks of symbols show the fits from Figure 12 (lower row) for galaxies in three different luminosity bins. The mean slope and zero point for the evolution of Milky Way stars are in good agreement with the overall metallicity and rate of enrichment for distant galaxies.

Fig. 15.— Fig. 13 of Kobulnicky & Kewley (2004, ApJ, 617, 240).

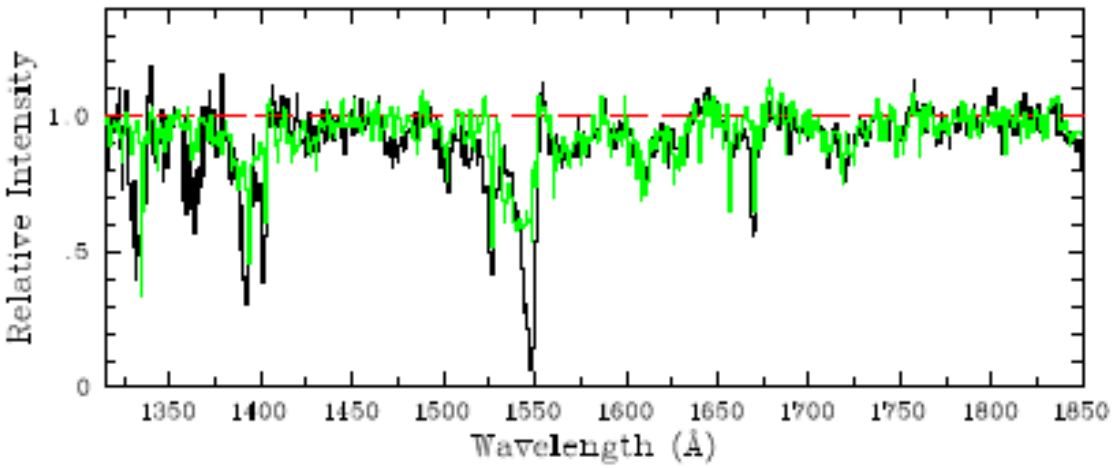

FIG. 5.— Comparison between the observed far-UV spectrum of Q1307-BM1163 (black histogram), normalized to the continuum and reduced to rest-frame wavelengths, and the simplest model spectrum produced with the population synthesis code *Starburst99*, one which assumes continuous star formation, solar metallicity, and a Salpeter IMF (green or gray histogram). The model's match to the data is remarkably good—the features which are not reproduced in the *Starburst99* composite stellar spectrum are in most cases interstellar absorption lines.

Fig. 16.— Fig. 5 of Steidel et al (2004),.

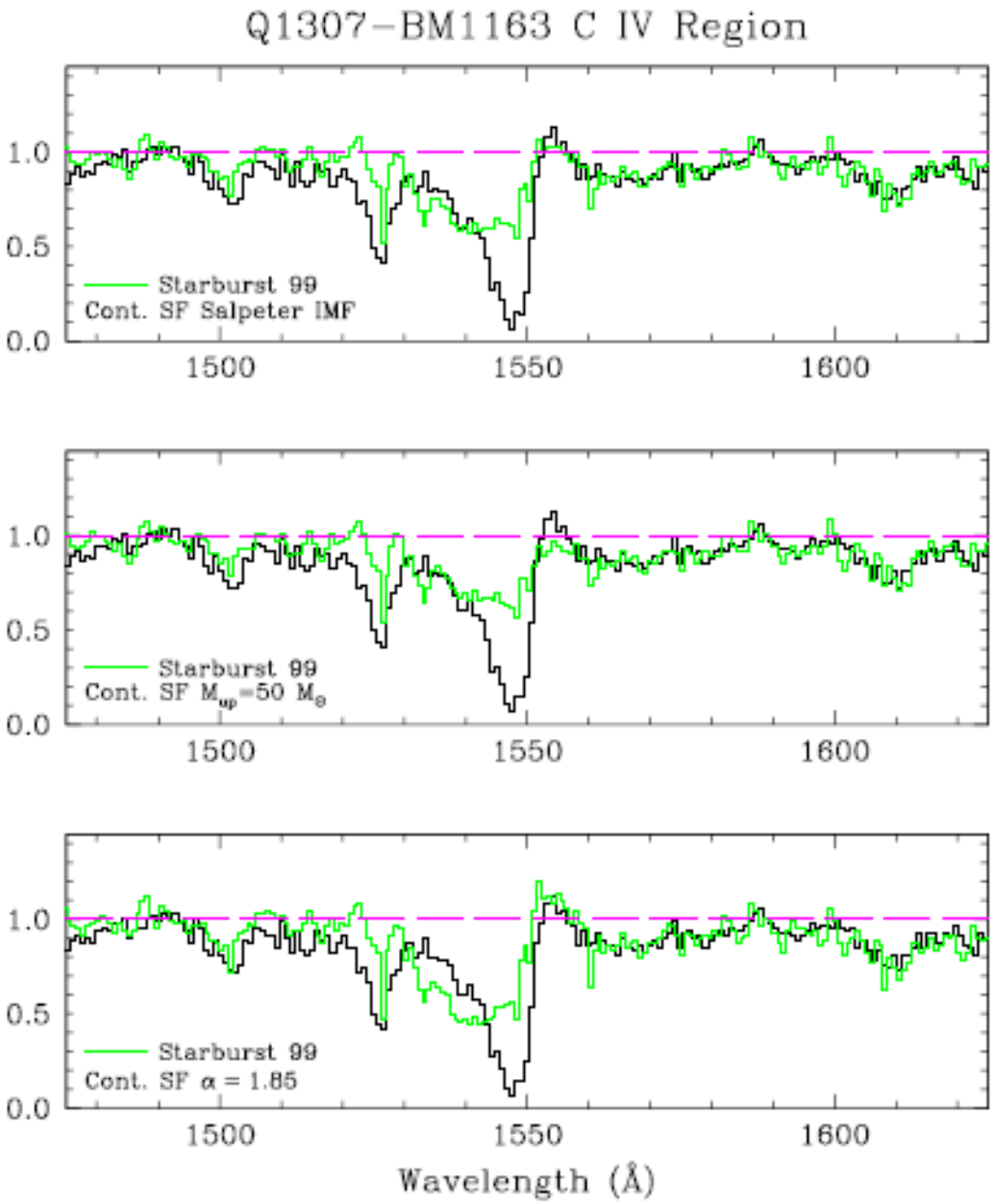

FIG. 6.— Sensitivity of the C IV P-Cygni profile to the upper end of the IMF. Black histogram: portion of the observed spectrum of Q1307-BM1163; green (or gray) histogram: model spectra produced by *Starburst99* with, respectively, a standard Salpeter IMF (top panel), an IMF lacking stars more massive than $50M_{\odot}$ (middle panel), and an IMF flatter than Salpeter (bottom panel). These changes were deliberately chosen to be relatively small, to illustrate the fact that it is possible to discriminate between them on the basis of even a relatively short exposure spectrum of this galaxy. Overall, there is no evidence for a departure from the standard Salpeter IMF at the upper end of the mass distribution of stars in Q1307-BM1163.

Fig. 17.— Fig. 6 of Steidel et al (2004). .

1.4. Metallicity - Luminosity at High Redshift

At higher redshifts Erb, Shapley, Pettini et al (2006) observed a sample of Lyman break galaxies in the near-IR, where they could detect Hα and NII features in emission by constructing composite spectra over six bins in luminosity. They find that Lyman break galaxies of a fixed luminosity are even more metal-poor than local galaxies. They find a $M - Z$ relation for oxygen among Lyman break galaxies at mean z of 2. At this redshift, there are large variations in rest-frame optical M/L due to variations in the star formation rate affecting the UV continuum, and the calibration for UV stellar photospheric features or UV ISM absorption to metallicity is not well understood at present (see Erb 2010 for details). So the best approach is to move into the near-IR, where the normal optical low redshift techniques and calibrations can be used.

Erb et al (2006) discuss how to transform luminosity into stellar mass. They use the star formation rate density to deduce the gas fraction. They find that the gas fraction increases as the stellar mass decreases, and the median gas fraction is significantly larger than is found in local star-forming galaxies. They suggest tht the outflow rate in these LBG galaxies is very high, $\sim$4 times the star formation rate. Combining the gas fractions with the observed metallicities enables them to calculate the effective yield.

High quality spectra are necessary for analysis of metallicity. For individual galaxies at high redshift, this is only possible if they are boosted by gravitational lensing. The IGM can be probed as their absorption features are seen against a very bright background from a distant QSO or some other bright distant source.

Pettini, Rix, Steidel et al (2002) observed a gravitationally lensed LBG with $z = 2.73$ to derive chemical abundances from 48 ISM absorption lines arising from H, C, N, O, Mg, Si, P, S, Mn, Fe, Ni and Zn. At this high redshift, Mg, Si, and S all give abundances about 2/5 of Solar. The galaxy seems to be chemically young (age about 300 Myr), which is

consistent with it's high redshift. The star formation rate is high, 40 $M_\odot$/yr.

SNR considerations suggest stacking of spectra of many similar galaxies to extend this work. Fig. 18 shows a composite spectrum of 321 $z \sim 3$ Lyman break galaxies from the sample of Steidel and collaborators (obtained over perhaps 100 nights of Keck time with LRIS) made by Alice Shapley (Fig. 3 of Kornei, Shapley, Erb, Steidel, Reddy, Pettini & Bogosavljevic, 2010, ApJ, in press). Most of the absorption lines arise from the ISM in the high redshift galaxy, only a few arise from its stellar population.

It is very clear that luminous high redshift galaxies are significantly enriched, with metallicities well above those of the DLAs at the same redshift, and at a given metallicity, high redshift galaxies are significantly more luminous that their local counterparts. Massive galaxies ($M > 10^{11}$ $M_\odot$) at $z \sim 2$ have approximately solar metallicity.

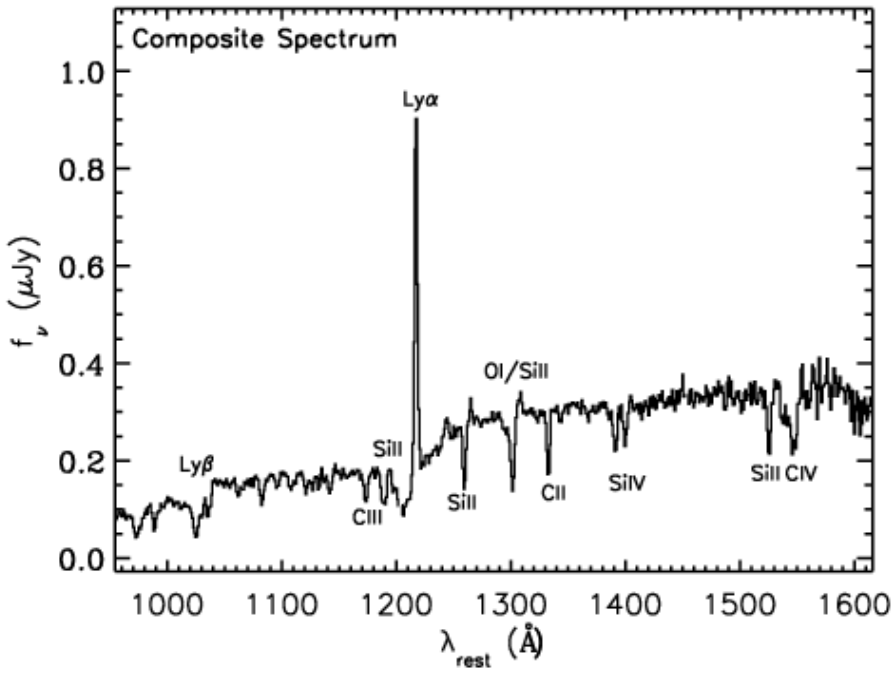

FIG. 4.— Composite rest-frame spectrum assembled from one-dimensional, flux-calibrated spectra (§2.4). Lyα appears in strong emission and Lyβ is prominent at 1026 Å. Photospheric features (e.g., CIII λ1176) and both low- (e.g., SiII $\lambda\lambda$1190,1193, SiII λ1260, OI+SiII λ1303, CII λ1334, and SiII λ1527) and high- (e.g., SiIV $\lambda\lambda$1393,1402 and CIV λ1549) ionization absorption lines are visible in this high signal-to-noise composite.

Fig. 18.— Fig. 3 of Kornei, Shapley, Erb, Steidel, Reddy, Pettini & Bogosavljevic, 2010, ApJ, in press

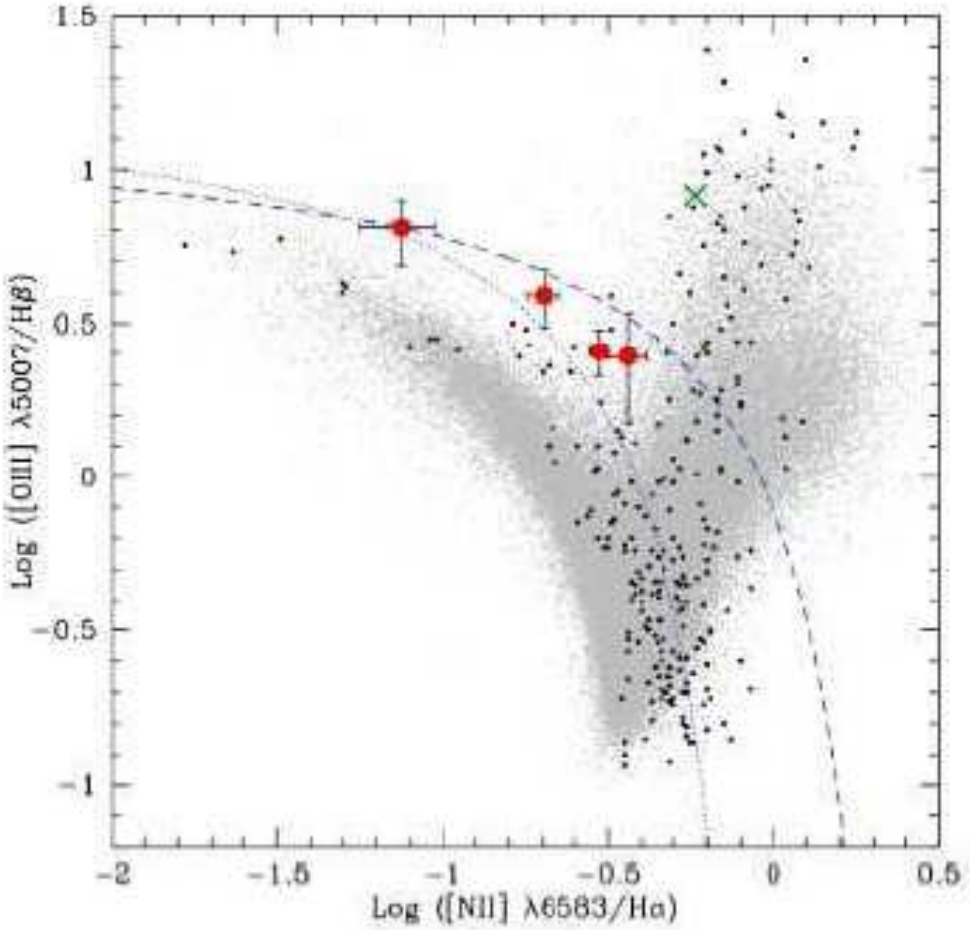

FIG. 1.— The [O III]/Hβ vs. [N II]/Hα diagnostic diagram. The four galaxies in our sample for which we have measurements of all four lines are shown by the large red circles. The $z = 2.2$ galaxy discussed by van Dokkum et al. (2005), which shows evidence of an AGN or shock ionization by a wind, is shown by the green $\times$. The small grey points represent $\sim 96,000$ objects from the SDSS, and the small black points are the local starburst galaxies studied by Kewley et al. (2001b). The dashed line shows the maximum theoretical starburst line of Kewley et al. (2001a); for realistic combinations of metallicity and ionization parameter, star-forming galaxies fall below and to the left of this line. The dotted line is a similar, empirical determination by Kauffmann et al. (2003).

Fig. 19.— Fig. 1 of Erb, Shapley, Pettini, Steidel, Reddy, & Adelberger, 2006 ApJ,644, 813.

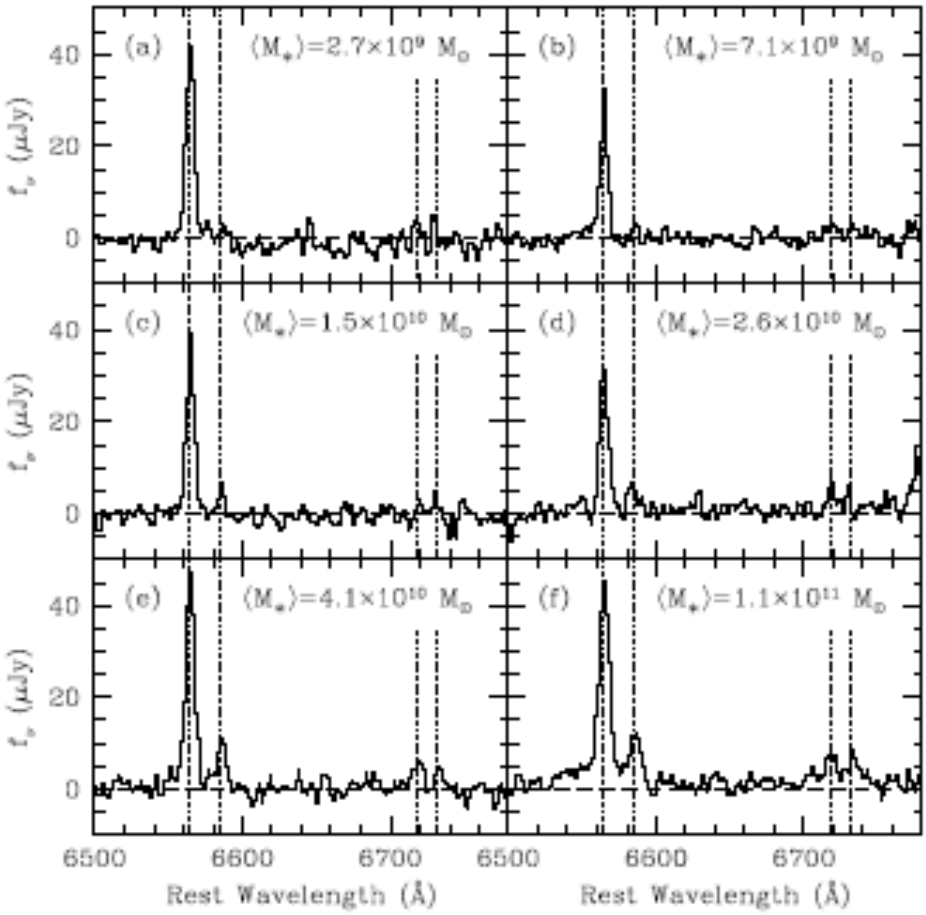

FIG. 2.— The composite NIRSPEC spectra of the 87 galaxies in our sample, divided into six bins of 14 or 15 objects each by increasing stellar mass (panels *a* through *f*). The spectra are labeled with the mean stellar mass in each bin, and the Hα, [N II], and [S II] lines are marked with dotted lines (left to right respectively). The increase in the strength of [N II] with stellar mass can be seen clearly. The density-sensitive [S II] lines, while weak, indicate a typical electron density of $n_e \sim 500$ cm^{-3}, with no significant dependence on mass; this is a value comparable to that seen in local starburst galaxies (Kewley et al. 2001b).

Fig. 20.— Fig. 2 of Erb, Shapley, Pettini, Steidel, Reddy, & Adelberger, 2006 ApJ,644, 813.

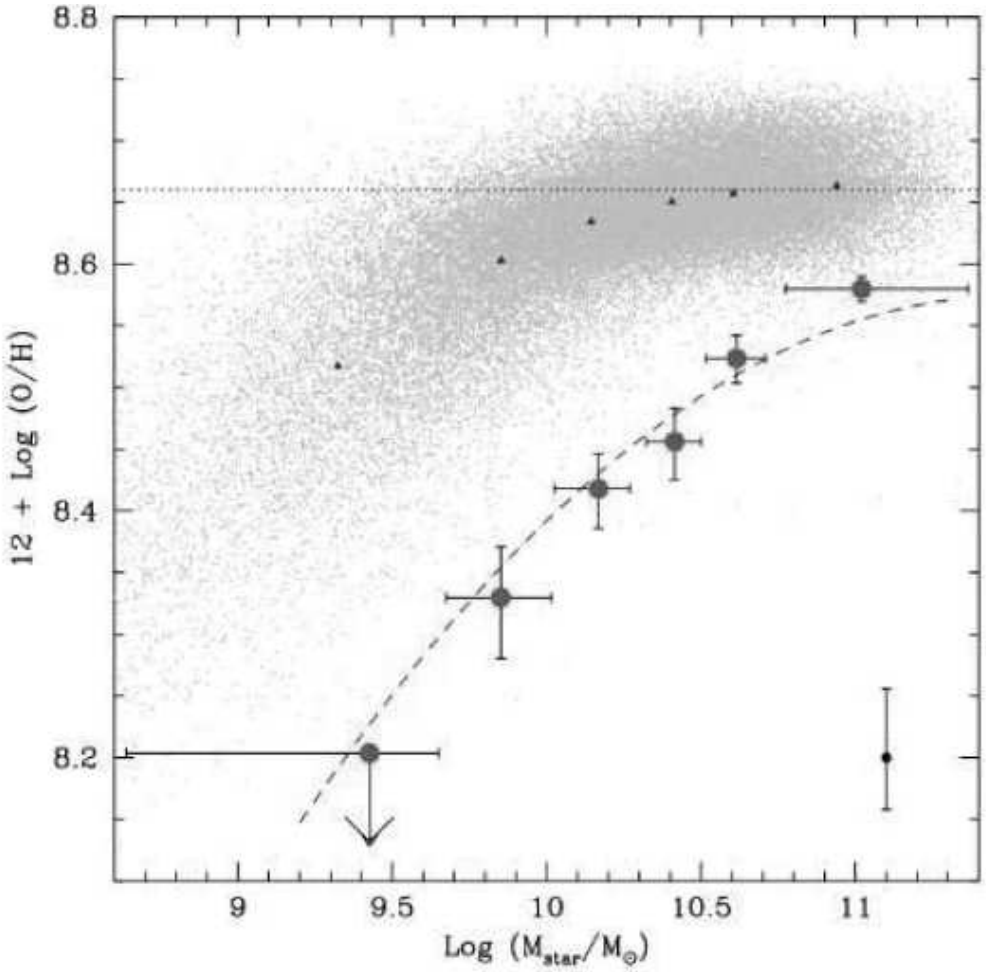

FIG. 3.— The observed relation between stellar mass and oxygen abundance at $z \sim 2$ is shown by the large red circles. Each point represents the average value of 14 or 15 galaxies, with the metallicity estimated from the [N II]/Hα ratio of their composite spectrum. Horizontal bars indicate the range of stellar masses in each bin, while the vertical error bars show the uncertainty in the [N II]/Hα ratio. The additional error bar in the lower right corner shows the additional uncertainty in the $N2$ calibration itself. The dashed blue line is the best-fit mass-metallicity relation of Tremonti et al. (2004), shifted downward by 0.56 dex. The metallicities of different samples are best compared using the same calibration; we therefore show, with small grey points, the metallicities of the $\sim 53,000$ SDSS galaxies of Tremonti et al. (2004) determined with the $N2$ index. Note that the [N II]/Hα ratio saturates near solar metallicity (the horizontal dotted line). The blue triangles indicate the mean metallicity of the SDSS galaxies in the same mass bins we use for our sample; using the more reliable, low metallicity bins, our galaxies are ~ 0.3 dex lower in metallicity at a given mass.

Fig. 21.— Fig. 3 of Erb, Shapley, Pettini, Steidel, Reddy, & Adelberger, 2006 ApJ,644, 813.

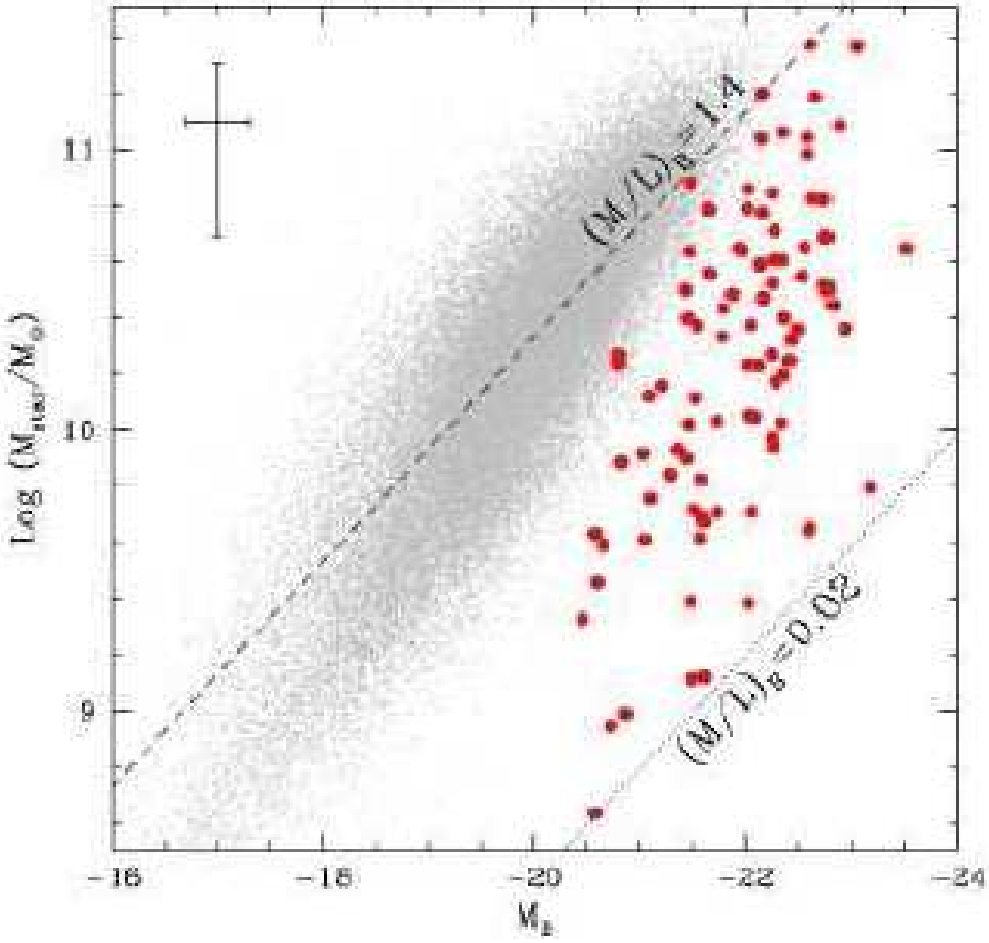

FIG. 7.— Absolute rest-frame B magnitude vs. stellar mass, for the individual galaxies in the $z \sim 2$ sample (large red circles) and the SDSS (small grey points). The dashed and dotted lines show constant mass-to-light ratios M/L; in the $z \sim 2$ sample, the total range in luminosity is narrow and M/L varies by a factor of ~ 70 at most luminosities, while for most SDSS galaxies, M/L varies by a factor of 2–5 at a given luminosity.

Fig. 22.— Fig. 7 of Erb, Shapley, Pettini, Steidel, Reddy, & Adelberger, 2006 ApJ,644, 813.

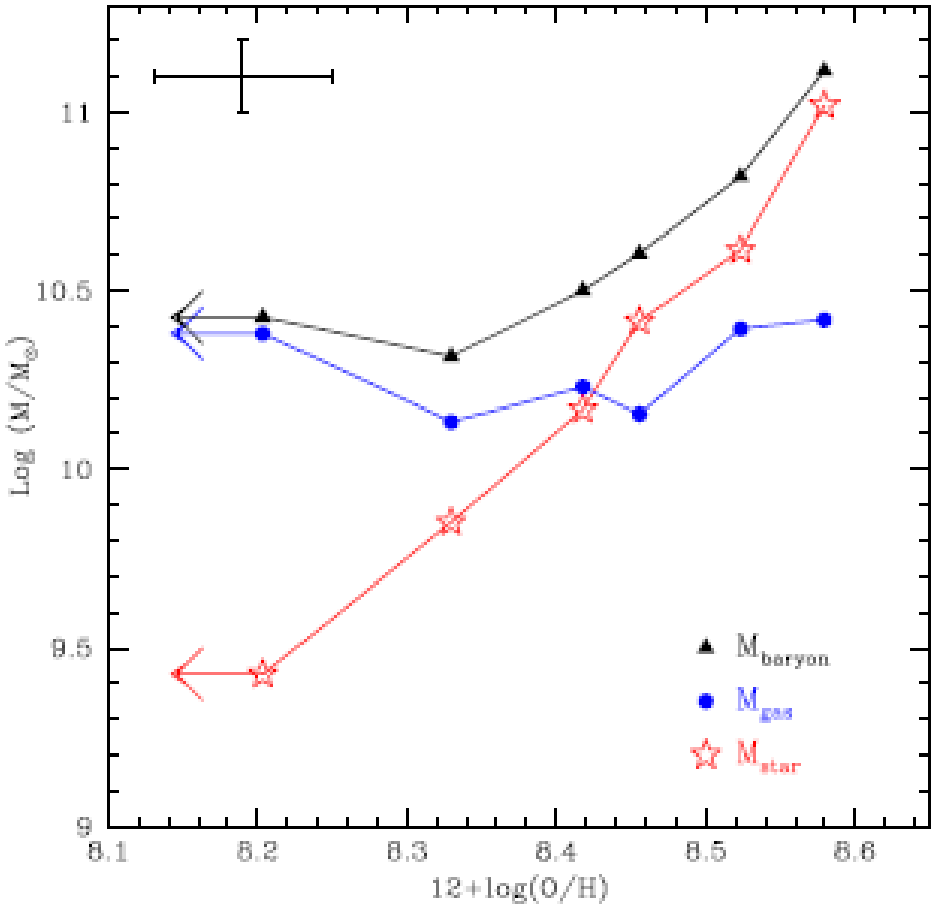

FIG. 8.— The variation of stellar, gas, and baryonic mass in each of the six bins with metallicity. Across the observed range in oxygen abundance, stellar mass increases strongly, baryonic mass increases weakly, and gas mass remains approximately constant. We thus see an increase in metallicity with decreasing gas fraction. The strong correlation between stellar mass and age means that metallicity also increases with the age of the stellar population. The error bars at upper left show typical uncertainties in gas and baryonic masses and metallicities; uncertainties in stellar masses are smaller.

Fig. 23.— Fig. 8 of Erb, Shapley, Pettini, Steidel, Reddy, & Adelberger, 2006 ApJ,644, 813.

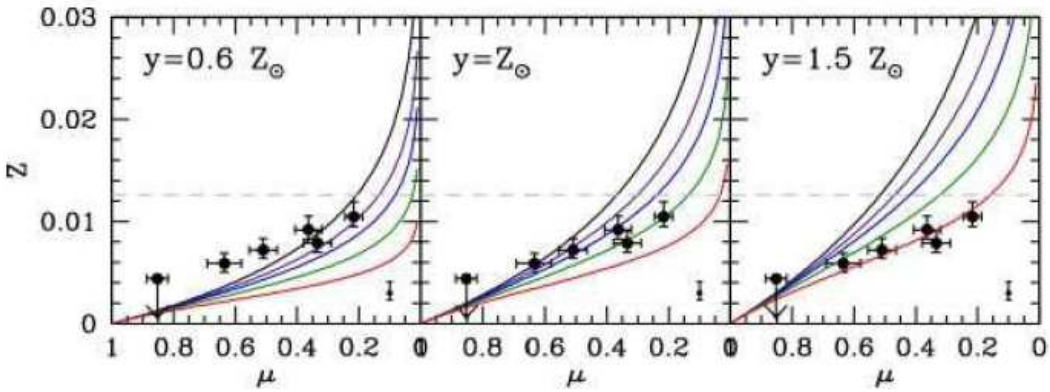

FIG. 9.— The points in each panel show the mean metallicity Z in each mass bin, plotted against the mean gas fraction μ. Gas fraction decreases from left to right, to show the increase in metallicity with decreasing gas fraction. The curves illustrate the variation of Z with μ for three different values of the true yield: from left to right, $y = 0.6\,Z_\odot$ (our observed effective yield), $y = Z_\odot$, and $y = 1.5\,Z_\odot$. Within each panel, the curves show varying values of the mass outflow rate $\dot{M}$, parameterized as a fraction f of the star formation rate. From top to bottom in each panel, the curves correspond to $f = 0$ (black; the closed box model), 0.5 (purple), 1 (blue), 2 (green) and 4 (red). The data are best matched by a model with supersolar yield and an outflow rate $\dot{M} \sim 4\times$SFR. The horizontal dashed grey line corresponds to solar metallicity, and the small error bar in the lower right corner of each panel shows the systematic uncertainty in the metallicity calibration.

Fig. 24.— Fig. 9 of Erb, Shapley, Pettini, Steidel, Reddy, & Adelberger, 2006 ApJ,644, 813.

1.5. "Old" Galaxies – 1. The Local Universe

"Old" galaxies are those with no current or even recent star formation, none within the past few Gyr at least. As they lack hot young stars, they tend to be "red" galaxies. Here one is forced to rely on the absorption line spectra. As an introduction to what might be achieved at high redshift, we begin with what can be achieved locally. Smith, Lucey, Hudson & Bridges (2009. MNRAS, 398, 119) have focused on the red-sequence galaxies in the nearby Coma cluster and the Shapley Supercluster of galaxies, studying galaxies of a wide luminosity (i.e. mass) range with moderate resolution but high accuracy spectra. A fixed aperture size is used for each galaxy, corresponding to a fixed physical size for each of the two galaxy clusters.

The Coma cluster of galaxies is the nearest virialized large cluster of galaxies with a well defined red sequence. It is roughly 10 times further away than the Virgo cluster of galaxies, with a recession velocity of $\sim$ 7000 km/sec.

The first point is there is a correlation for passively evolving galaxies [Fe/H] = $a_1 log\sigma - a_2 log(t_{SSP}) + a_3$, where t_{SSP} is the age since the single burst of star formation which characterizes a passively evolving galaxy and a_1, a_2, and a_3 are constants. The velocity dispersion σ is a proxy for the galaxy mass.

In this paper they try to establish similar correlations for the abundance ratios of C, N, Mg, and Ca with respect to [Fe/H]. They try fits with red luminosity σ, t_{SSP}, and [Fe/H], trying to minimize the residuals about the best linear fit.

They find that rather than a simple dependence on mass (parameterized by the velocity dispersion σ), a two parameter relation of the form [X/Fe] = $b_0 + b_1 log(\sigma) + b_2$ [Fe/H] seems to work well. For the α elements Mg and Ca, there is a positive correlation with velocity dispersion and an anti-correlation with [Fe/H]. For C and N, there is essentially no

correlation with [Fe/H], with $a_1 > 0$ and $a_2 \approx 0$. They try to explain this by a systematic variation of star-formation time-scale with σ, but fail to find any simple prescription that reproduces their observed trends. Irrespective of this, a comparison of the quality of their data with that for more distant "old" passively evolving galaxies is very illuminating and sobering.

A selection of figures from this paper is given below. Note that these authors have been careful and calculated the expected correlation of each relation just from the correlations among the errors in various parameters, which are not competely independent.

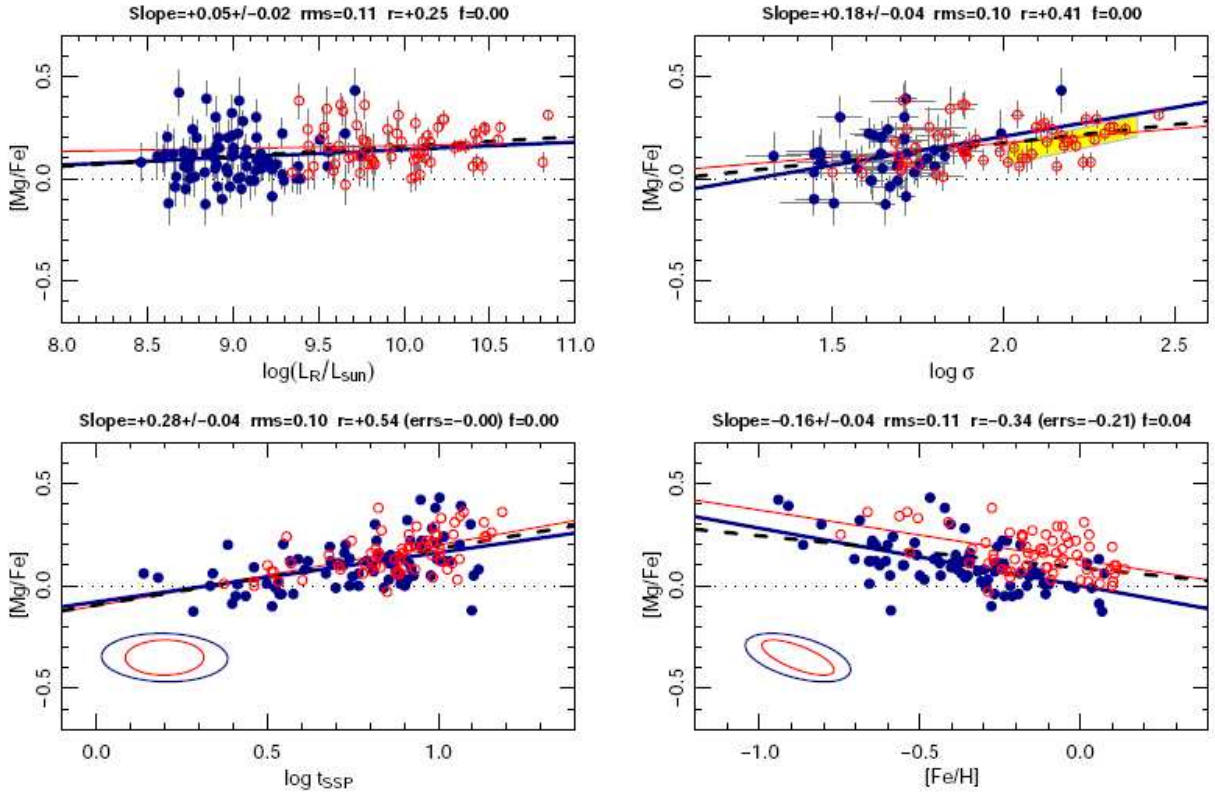

Fig. 25.— The Coma cluster and Shapley supercluster "old" red galaxy samples: [Mg/Fe] as a function of various integrated light galaxy parameters, red luminosity (top left), velocity dispersion of stars (top right), SSP age (lower left) and metallicity [Fe/H] (lower right). The Coma galaxies are shown as blue filled symbols, the Shapley galaxies with red open symbols. The yellow track in the upper right panel is the mean trend for giant galaxies. In two panels a typical error ellipse for each of the two clusters is shown at the lower left. The top label of each panel gives the parameters of the fit, the slope, the rms scatter for the fit to the combined sample. The product-moment correlation coefficient is r. The probability f of exceeding this r value by chance is computed for just the Shapley data. The r expected from correlated errors alone is given in parentheses. The separation between Coma and Shapley galaxies in the lower right panel arises because the Shapley galaxies in the mean have much higher velocity dispersions. Fig. 1 of Smith et al (2009, MNRAS, 398, 119).

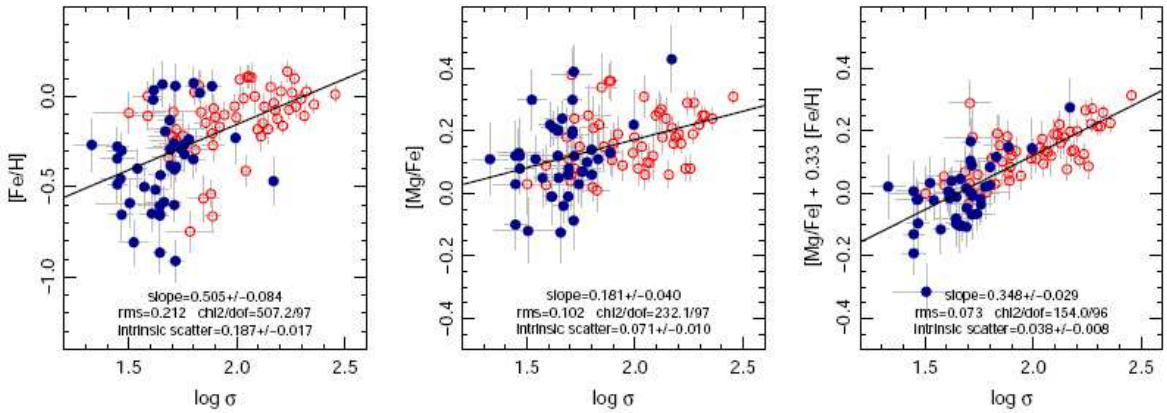

Figure 2. Left: the Fe/H–σ correlation for the combined Shapley (red) and Coma (blue) sample. Although these parameters are correlated, our sample covers sufficient baseline in each parameter that correlations primarily with σ can be distinguished from correlations primarily with Fe/H. Centre: the traditional Mg/Fe–σ relation. Right: the σ-projection of the X-plane for Mg. The vertical errorbars account for the anti-correlated errors in Mg/Fe and Fe/H. Introducing the additional Fe/H dependence reduces the total rms scatter is from 0.10 dex to 0.07 dex (a factor of two in the variance), and the intrinsic scatter from 0.07 dex to 0.04 dex (a factor of three in variance). Note that the reduction of scatter can be appreciated in both the Shapley and the Coma sample taken individually.

Fig. 26.— The Coma cluster and Shapley supercluster "old" red galaxy samples: [Fe/H] and [Mg/Fe] as a function of the integrated light velocity dispersion σ. The scatter of the relation is minimized when a combination of [Fe/H] and [Mg/Fe] is used. Fig. 2 of Smith et al (2009, MNRAS, 398, 119).

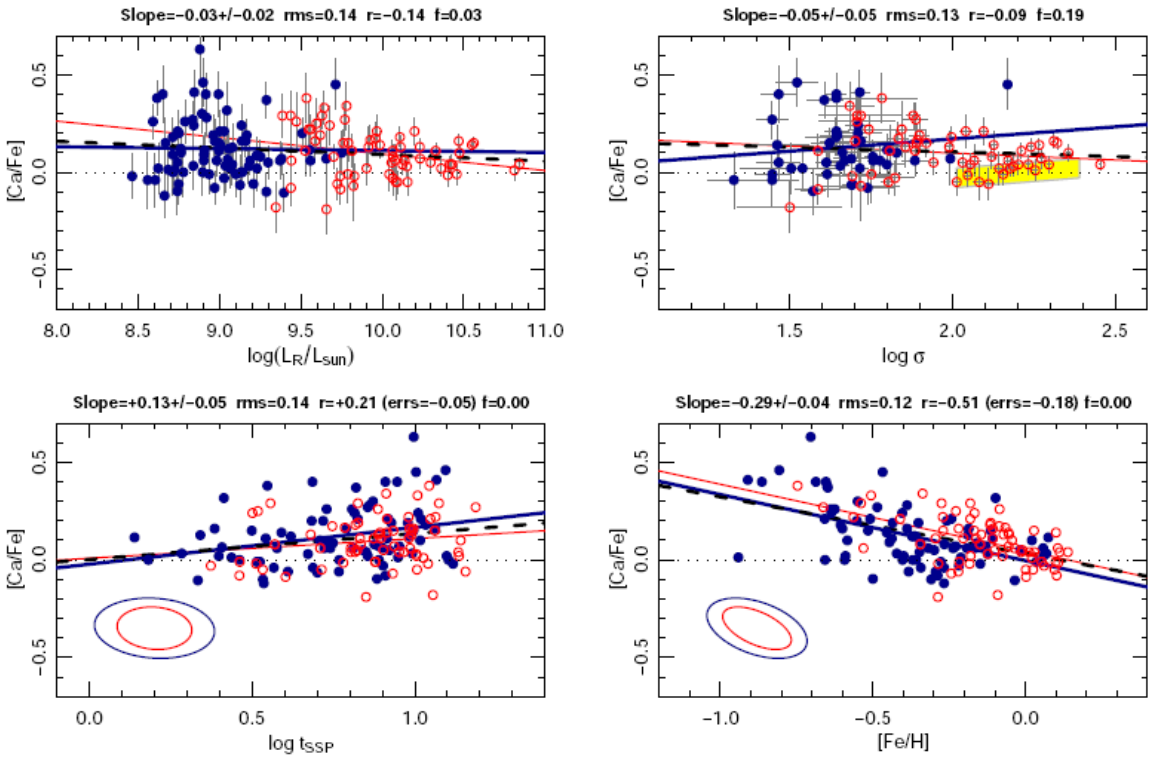

Figure 3. Correlations for Ca/Fe. The behaviour is qualitatively similar to that of Mg/Fe in Figure 1, except for the absence of correlation with σ. Symbols and annotations as in Figure 1.

Fig. 27.— The Coma cluster and Shapley supercluster "old" red galaxy samples: [Ca/Fe] as a function of various integrated light galaxy parameters. Note that [C/Fe] depends on [Fe/H] and on t_{SSP}, with little dependence on σ. Fig. 3 of Smith et al (2009, MNRAS, 398, 119).

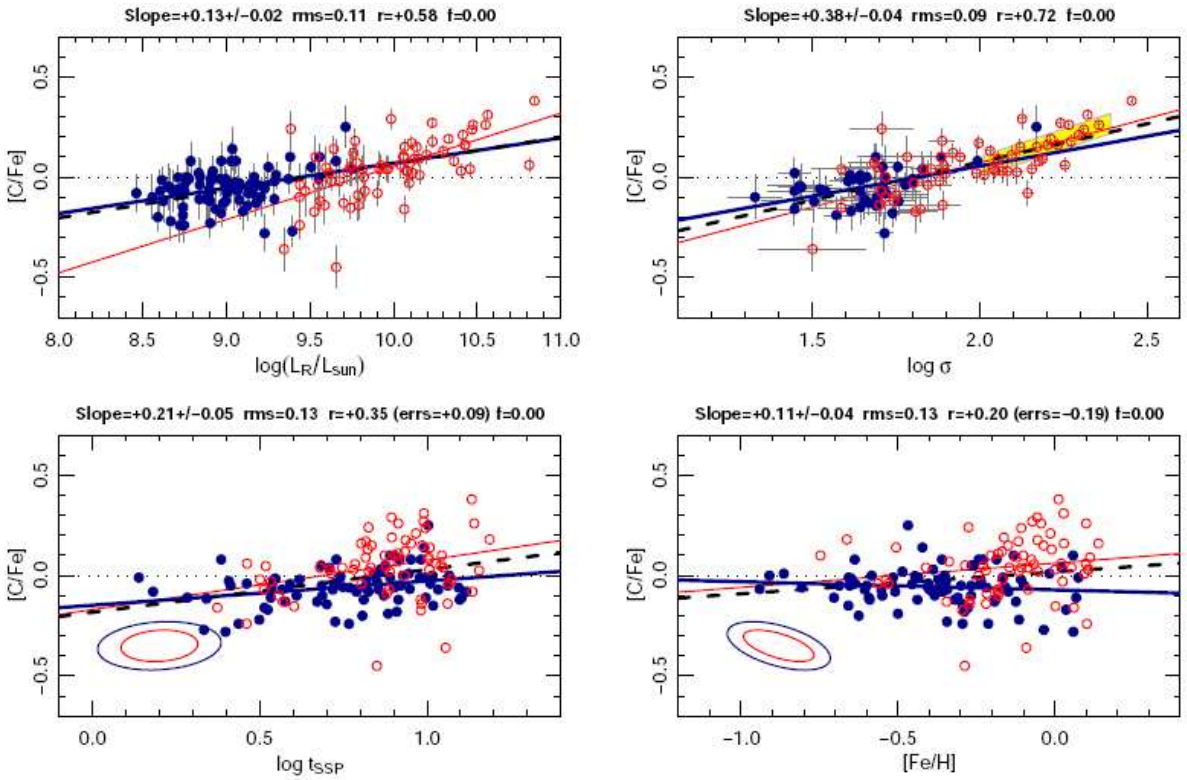

Figure 5. Correlations for C/Fe. Note the steep and tight correlation with velocity dispersion, and the absence of dependence on Fe/H. The latter is quite unlike the case for the α elements (Figures 1 and 3). Symbols and annotations as in Figure 1.

Fig. 28.— The Coma cluster and Shapley supercluster "old" red galaxy samples: [C/Fe] as a function of various integrated light galaxy parameters. Note that [C/Fe] does not appear to depend on [Fe/H]. Fig. 5 of Smith et al (2009, MNRAS, 398, 119).

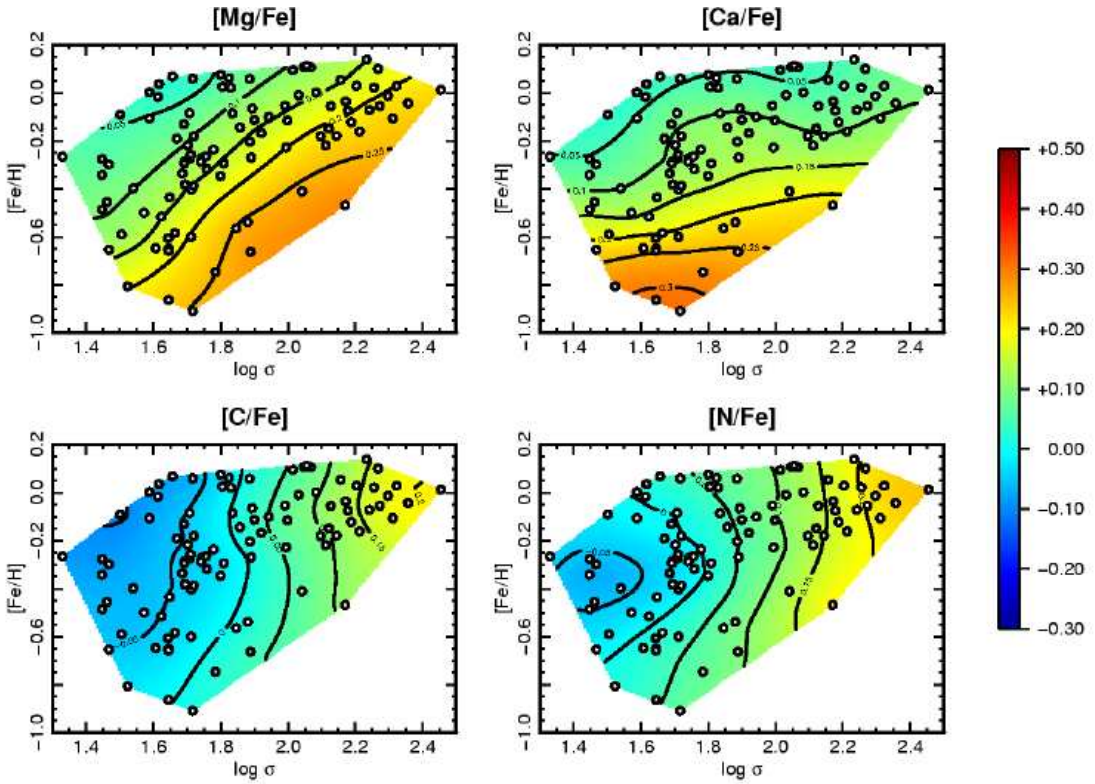

Figure 9. The abundance ratios on the Fe–σ plane. The points show the Fe/H–σ relation for the combined Coma and Shapley galaxy sample, as in the left panel of Figure 2. The colour shading and contours were derived by heavily smoothing the X/Fe ratios onto this plane using a Kriging model (see e.g. Cressie 1993). Contours are spaced at 0.05 dex intervals. Note the distinction between C and N, where the near-vertical contour indicate dependence only on σ, and Mg and Ca, where the contours are inclined and show a strong dependence on Fe/H.

Fig. 29.— The Coma cluster and Shapley supercluster "old" red galaxy samples: [Mg, Ca, C, N/Fe] ratios are contoured onto the [Fe/H] – σ plane. The C and N/Fe contours are nearly vertical, suggesting a dependence on σ but not on [Fe/H]. The contours for [Mg, Ca/Fe] are inclined and show a dependence on both σ and [Fe/H] of the galaxy. Fig. 9 of Smith et al (2009, MNRAS, 398, 119).

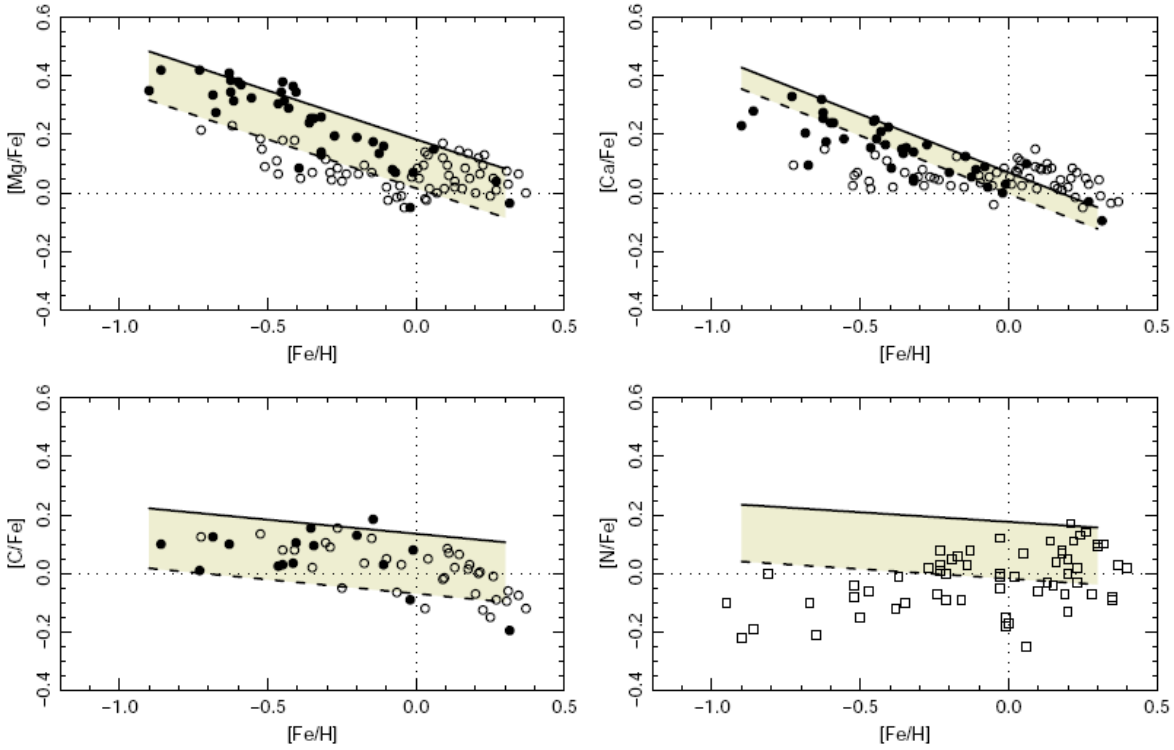

Figure 10. Comparing abundance ratio data for milky way stars (points) and passive galaxies (lines and shading). The filled and open circles indicate thick and thin disk stars, respectively, from Bensby et al. (2005). In the N/Fe panel, squares show stars from Ecuvillon et al. (2004) and Israelian et al. (2004). In each panel, the X-plane fits (Table 2) have been used to derive the mean X/Fe–Fe/H relation for galaxies of velocity dispersion $\sigma = 50\,\mathrm{km\,s^{-1}}$ and $\sigma = 150\,\mathrm{km\,s^{-1}}$ (dashed and solid black lines, respectively). The agreement between the stellar data and the external galaxies suggests a degree of similarity in their enrichment processes.

Fig. 30.— The trends of abundance ratios [Mg, Ca, C, N/Fe] vs [Fe/H]in old galaxies of the Coma cluster and Shapeley supercluster over a range of luminosities are shown. Also shown are the same trends for Milky Way thin and thick disk stars. Overall, except for N, the relations are very similar, suggesting similar chemical enrichment processes. Fig. 10 of Smith et al (2009, MNRAS, 398, 119).

1.6. "Old" Galaxies – 2. The Distant Universe

How can one find "old" passively evolving galaxies in the distant universe ? Any selection by color (looking for "red" galaxies) faces eliminating numerous late type stars as sample interlopers. Furthermore discrimination between heavily reddened, intrinsically blue star-forming galaxies versus genuinely "old" galaxies is not always feasible. This is much more difficult terrain, see, e.g. Brammer, Whitaker, van Dokkum etal, 2010, ApJ (the dead sequence...)

The group of Marijn Franx (including van Dokkum) use their very deep ground-based near-IR photometry to search for galaxies at $z \sim 2$ which are "old", without recent star formation. These galaxies are typically more massive than star-forming Lyman break galaxies.

Up to $z \sim 0.8$ where the standard optical absorption features can be observed, there is a fair amount of data in metallicity of luminous red galaxies (they are in general quite metal-rich), as well as on their broad band colors, luminosities, morphology of such galaxies, star formation rates, etc. Beyond that redshift, while data exists on morphology, luminosity, star formation rates etc. there is very little information on metallicity.

A series of figures from van Dokkum, Whitaker, Brammer et al (ApJ, in press, 2010) (arXiv:0912.0514) illustrates the state of the art for distant galaxies without strong emission lines. Their sample is galaxies with a constant number density of $2 \times 10^{-4}/\mathrm{Mpc}^{-3}$, which locally have a typical stellar mass of $3 \times 10^{11} M_{\odot}$, and are in halos of mean mass $5 \times 10^{13}\ M_{\odot}$. Locally these are the central galaxies of massive groups. They have multi-band photometry from 3500 Å through the near-infrared using the new wide field IR camera at NOAO (NEWFIRM), combined with Spitzer IRAC and MIPS imaging. They use photometric redshifts, which given their very wide wavelength coverage and accurate photometry, should be OK. There is essentially no detailed spectroscopy of galaxies in their sample.

They show that the stellar mass of galaxies at their fixed number density has increased by a factor of $\sim$2 since $z = 2$, and that the buildup of stars has occured in the outer parts of the galaxies rather than in their dense central regions. Thus these galaxies have changed the surface brightness profile with redshift. They suggest that the growth in total mass is dominated by mergers, as the star formation rates are not high enough to accomplish this.

The difficulty of obtaining spectra for red galaxies with no star-formation at $z \sim 2$ is illustrated by Fig. 37 which is a 29 hour exposure on the Gemini South telescope, and the S/N is pretty low. Wilson, Muzzin, Yee et al (2009) illustrate what is possible at a more modest redshift of $z \sim 1.3$, where the key spectral features around the Balmer break begin to shift into the red far enough to be in regions of strong night sky emission from molecules in the Earth's atmosphere.

Comparing these figures to those for the Coma cluster indicates how badly we need larger collecting areas, i.e. the next generation of big telescopes, to study galaxies in the distant universe.

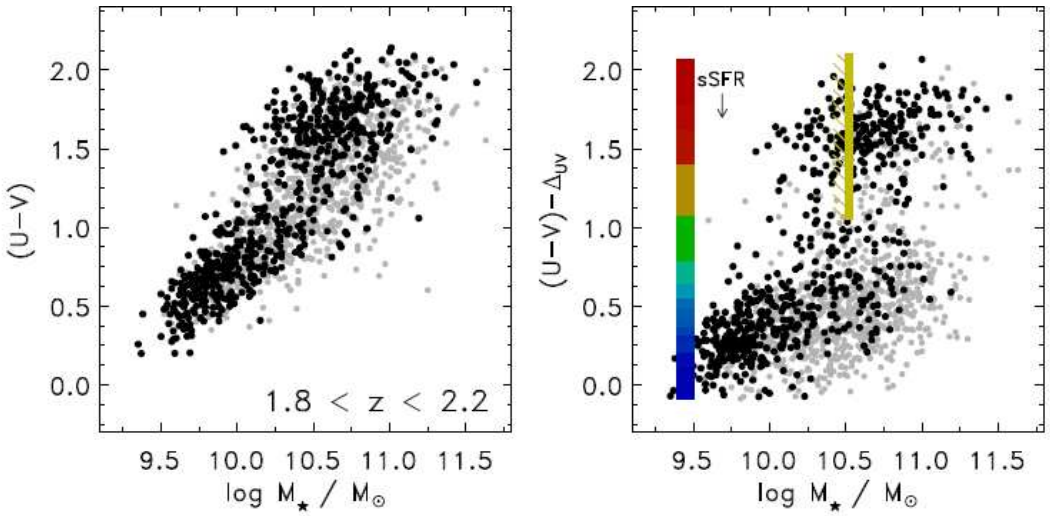

FIG. 4.— The color-mass relation at $1.8 < z < 2.2$. The $U - V$ color in the right panel is corrected for reddening with the factor from Eq. 2. Objects detected at 24 μm are shown as filled gray circles. The hatched region indicates the approximate 90% completeness limit for red-sequence objects at $z = 2$. Due to the reddening correction, the completeness limit for blue galaxies is more difficult to estimate. The colorbar in the right panel shows the median sSFR as a function of dust-corrected color, with the same coding as Figure 3.

Fig. 31.— Fig. 4 of Brammer, Whitaker, van Dokkum et al, 2010, ApJ, arXiv:0910.2227.

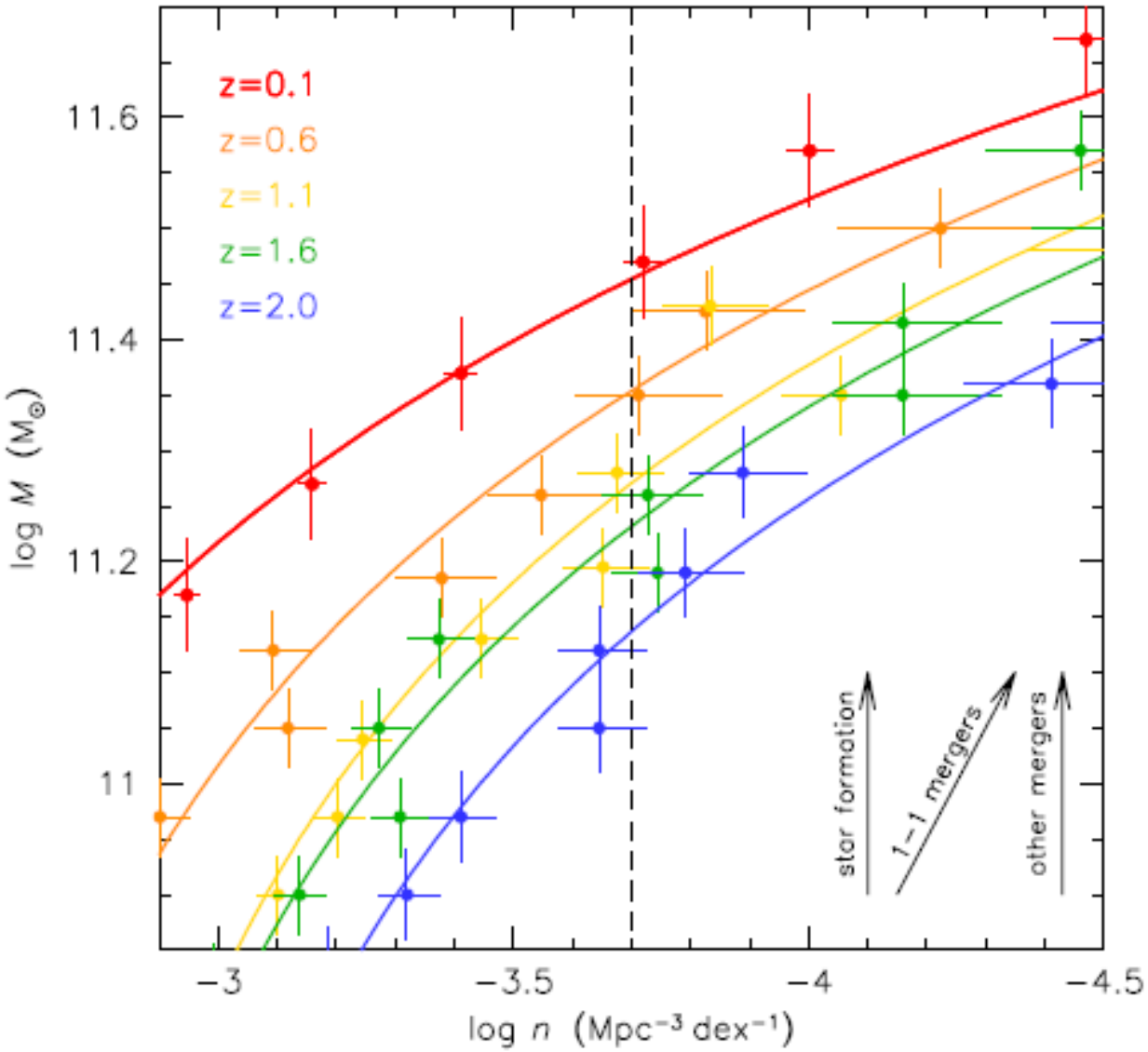

FIG. 1.— Evolution of the stellar mass – number density relation at $0 < z < 2$, derived from Cole et al. (2001) and the NEWFIRM Medium Band Survey data. Arrows indicate the expected evolution for star formation, equal mass mergers, and mergers with mass ratios < 1. For most astrophysical processes the most massive galaxies are expected to evolve along lines of constant number density, not constant mass. The dashed line shows the selection applied in this study: a constant number density of $n = 2 \times 10^{-4}$ Mpc^{-3}.

Fig. 32.— Fig. 1 of van Dokkum, Whitaker, Brammer et al (ApJ, in press, 2010). (arXiv:0912.0514).

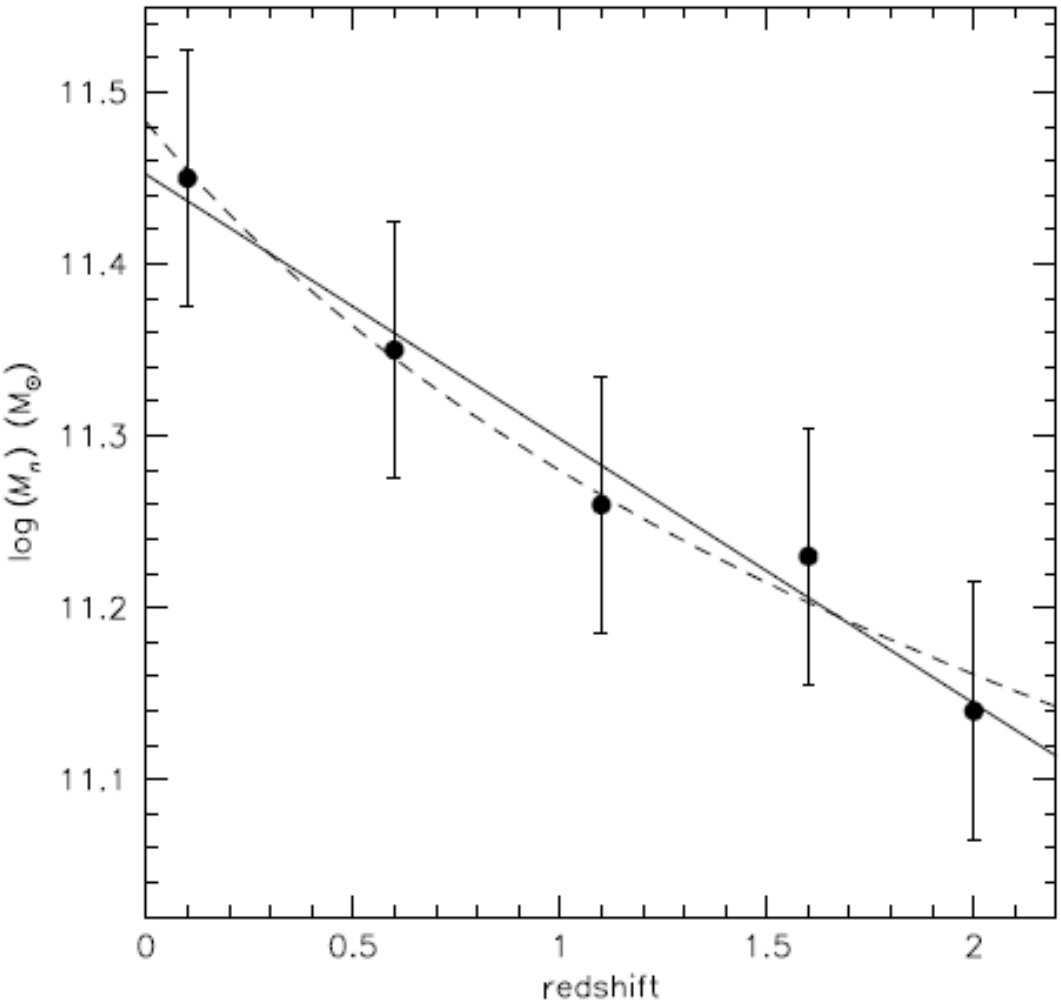

FIG. 2.— The stellar mass of galaxies with a number density of 2×10^{-4} Mpc^{-3}, as a function of redshift. Errorbars are based on estimates of the amount of light that may be missed in our photometry; random errors are negligible. The observed mass evolution is very regular with small scatter. The solid line is a simple linear fit to the data, of the form $\log M_n = 11.45 - 0.15z$. The dashed line has the form $\log M_n = 11.48 - 0.67 \log(1+z)$. The fits imply that galaxies with a stellar mass of 3×10^{11} M$_\odot$ today assembled ~ 50 % of their mass at $0 < z < 2$. We note that unknown systematic uncertainties in the derived stellar masses have been ignored.

Fig. 33.— Fig. 2 of van Dokkum, Whitaker, Brammer et al (ApJ, in press, 2010). (arXiv:0912.0514).

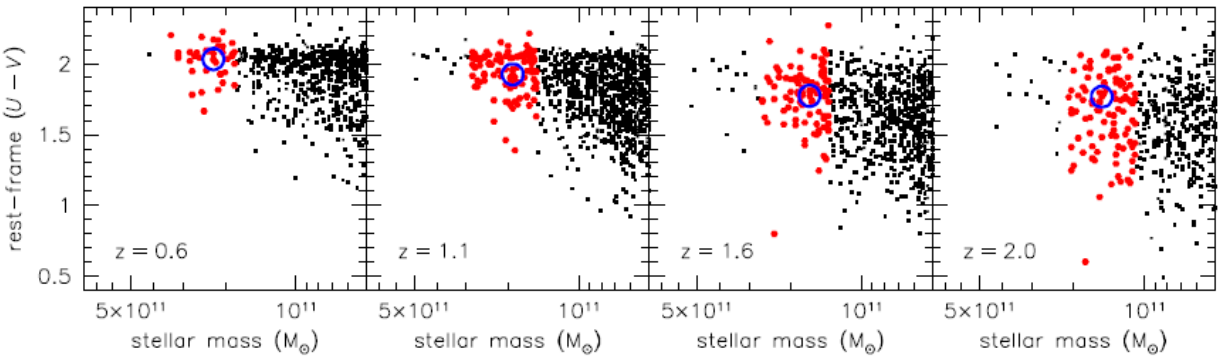

FIG. 3.— Rest-frame $U-V$ color versus mass for galaxies in the NMBS. In each redshift bin galaxies were selected in a ± 0.15 dex wide mass bin whose median mass is equal to M_n. Galaxies satisfying this criterion are highlighted in red. Out to $z \sim 1$ this selection includes mostly red galaxies. At higher redshifts an increasing fraction of the sample is blue. This is a real effect, and not due to photometric errors.

Fig. 34.— Figs. 3 of van Dokkum, Whitaker, Brammer et al (ApJ, in press, 2010). (arXiv:0912.0514).

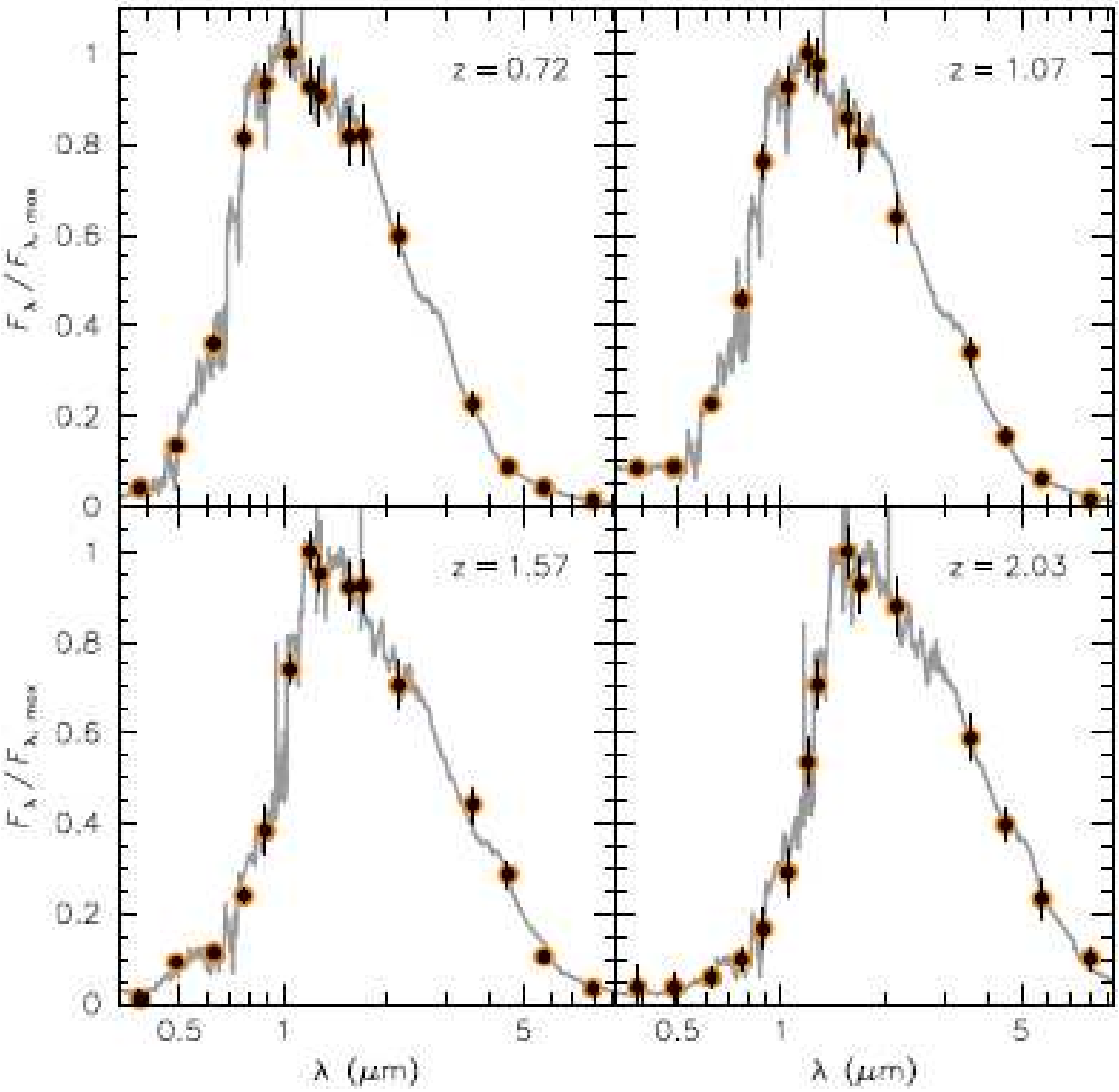

FIG. 4.— Spectral energy distributions of typical galaxies in the four redshift bins, illustrating the high quality of our photometric data. The locations of these galaxies in the color-mass plane are indicated by blue circles in Fig. 3. Data points are *u*, *g*, *r*, *i*, *z* from the Deep CFHT Legacy Survey, J_1, J_2, J_3, H_1, H_2, and K from the NMBS, and IRAC channel 1–4. The grey line shows the best-fitting EAZY template (Brammer et al. 2008). Note that the medium band filters are critical for determining the redshifts and SED shapes for galaxies in this mass and redshift range.

Fig. 35.— Figs. 4 of van Dokkum, Whitaker, Brammer et al (ApJ, in press, 2010). (arXiv:0912.0514).

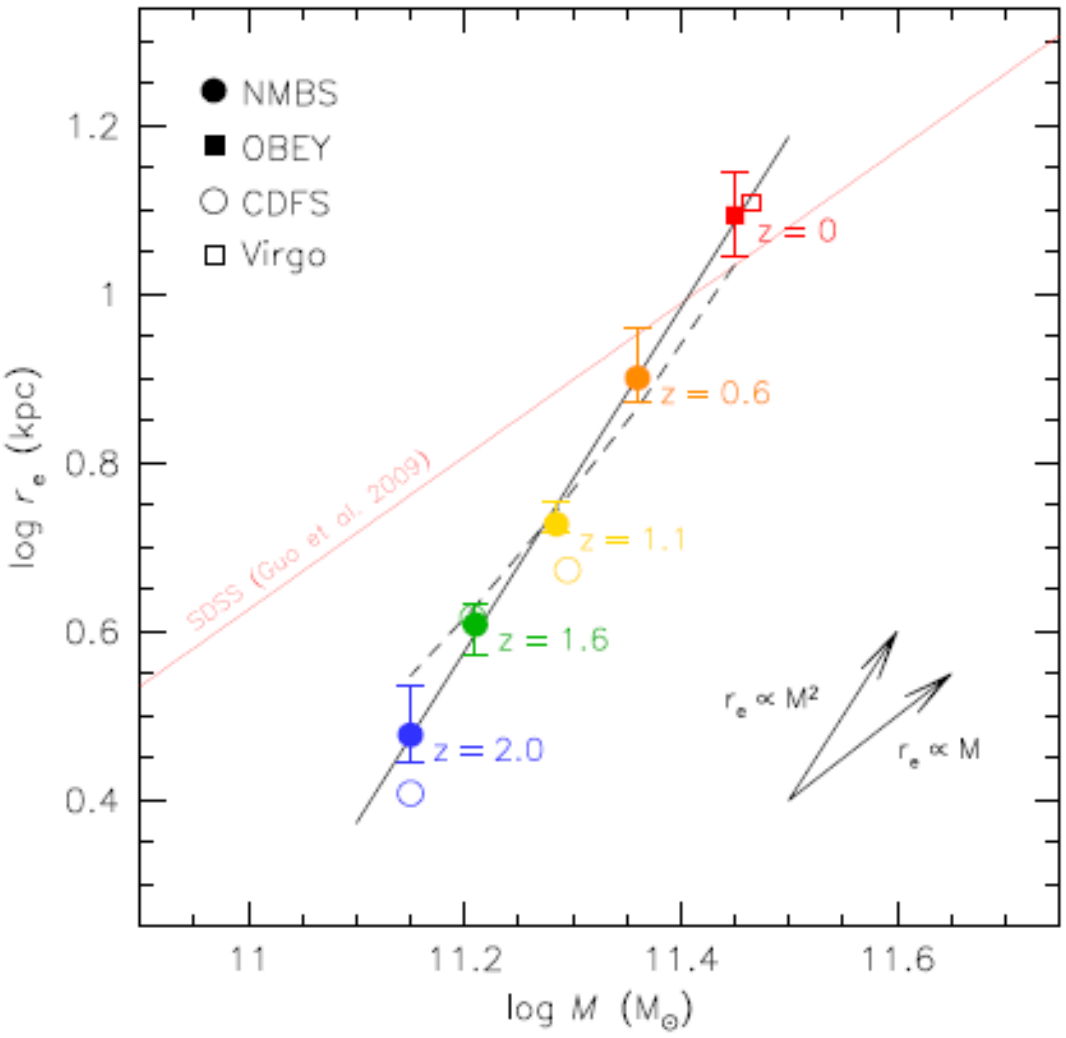

FIG. 8.— Evolution in the radius-mass plane. Our data are consistent with measurements for individual galaxies of the same masses and redshifts in the FIREWORKS CDF-South survey of Wuyts et al. (2008) and Franx et al. (2008) (open circles). Our $z = 0$ point from the OBEY survey (Tal et al. 2009) is consistent with data from Virgo ellipticals by Kormendy et al. (2009) and a recent determination of the mass-size relation in the SDSS (Guo et al. 2009). The evolution in effective radius is stronger than in mass: the solid line is a fit of the form $r_e \propto M^{2.04}$. The dashed line is the expected evolution of the effective radius for inside-out growth, calculated using Eq. 7 and the measured value of the Sersic index n at each redshift.

Fig. 36.— Figs. 8 of van Dokkum, Whitaker, Brammer et al (ApJ, in press, 2010). (arXiv:0912.0514).

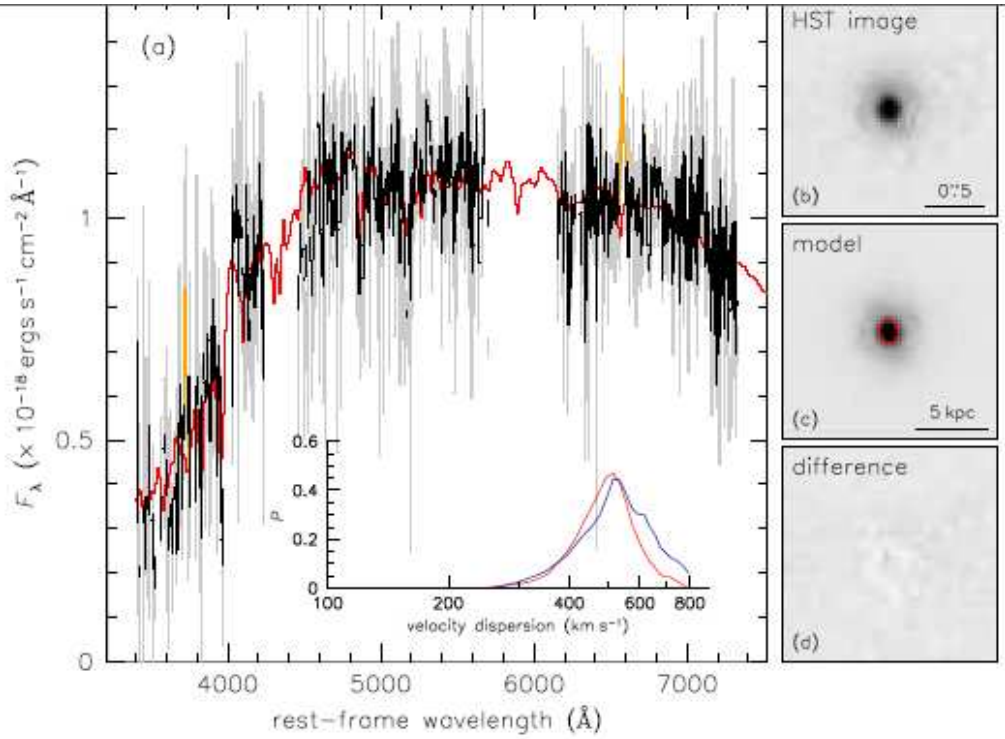

Figure 1 | Spectrum and HST images of 1255–0 at z = 2.186. **a**, Spectrum that was used to measure the velocity dispersion. Light grey shows the spectrum at a resolution of 5 Å (≈ 100 km s^{-1}), which was used for the actual measurement. A smoothed version of the same data (using a 25 Å boxcar filter) is shown in black. Regions around detected emission lines are shown in orange and were excluded from the fits. The most prominent absorption lines are Hβ at λ4861 Å and Mg at λ5172 Å. The best-fitting stellar population synthesis model,[14] smoothed to the best-fitting velocity dispersion, is shown in red. The inset shows the results of Monte Carlo simulations to determine the uncertainty in the best-fitting velocity dispersion. The curves show how often a dispersion of 510 km s^{-1} is measured given the true dispersion and noise. The two curves are for two different methods of simulating noise: shuffling the residuals of the fit in the wavelength direction (blue curve), and extracting "empty" 1D spectra from the 2D spectrum (red curve). **b-d**, The HST NICMOS2 image of the galaxy in the H_{160} filter, the best-fitting model of the galaxy (with the effective radius indicated in red), and the residual obtained by subtracting the model from the data. The galaxy is a single, very compact object with an effective radius of 0.78 kpc. Its coordinates are $\alpha = 12^{\rm h}54^{\rm m}59.6^{\rm s}$, $\delta = +01°11^{\rm m}30^{\rm s}$

Fig. 37.— Fig. 1 of van Dokkum, Kriek & Franx, 2009, Nature, 460, 717 (arXiv:0906.2778).

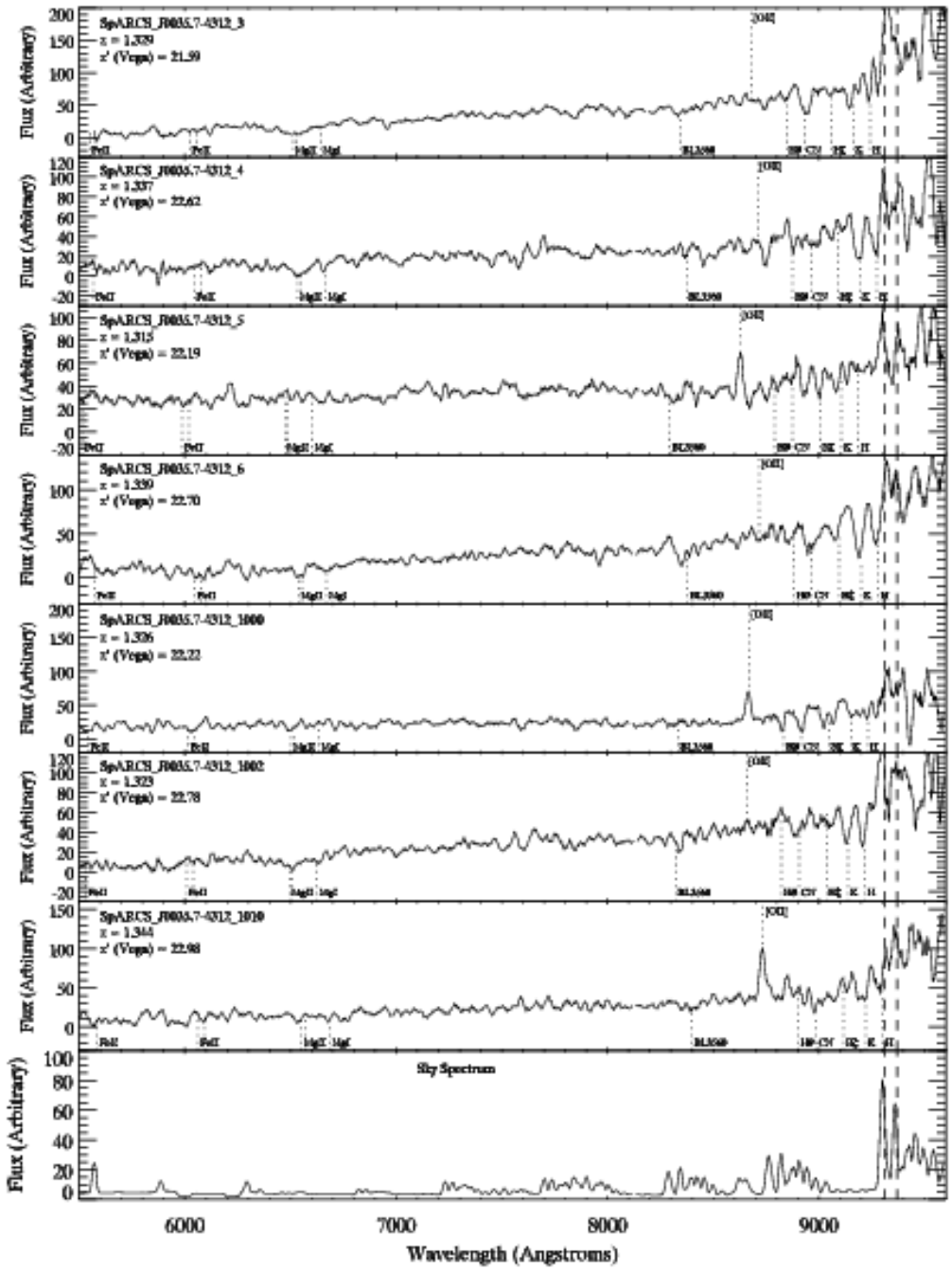

FIG. 3.— Spectra for a subsample of seven galaxies in cluster SpARCS J003550-431224 (see Table 2). The spectra have been smoothed ith a 7-pixel (11 Å) boxcar. The identified spectral features are marked. The lowermost panel shows the typical sky spectrum.

Fig. 38.— Fig. 3 of Wilson, Muzzin, Yee et al (ApJ,2009). (z=1.34 gal cluster).

1.7. Clusters vs Field

There is a strong difference in the population of the field versus clusters of galaxies at a given redshift, at least out to $z \sim 1.3$. First dicussed by Harvey Butcher and Gus Oemler in 1985 (ApJS, 57, 665), this has been known for many years.

Furthermore, the behavior of the "red" galaxies in massive clusters has been demonstrated to follow a sequence that agrees with passive stellar evolution. The colors of galaxies along this sequence at $z \sim 1$ require that the bulk of the stars in these galaxies formed at high-redshift, $z_f > 4$. See the many photometric studies by Adam Sanford, Mike Gladders and others for recent work.

The IRAC Shallow Cluster Survey (see Brodwin, Eisenhardt, Gonzalez et al, 2009) has a sample of 335 galaxy clusters and groups from $z = 0$ to $z = 2$ found by aplying the red cluster sequence technique to Spitzer IRAC images; 116 of them are expected to be at $z > 1$.

The cluster number density and auto-correlation function can be predicted from ΛCDM and compared to the observations.

The original formulation of the Butcher-Oemler (Butcher & Oemler 1978, ApJ, 219, 18) effect reflected the dominance of elliptical and S0 galaxies in the central regions of large clusters of galaxies compared to their paucity in the field, and the decreased fraction of S0s and elipticals to spiral galaxies within clusters as z increases. This was interpreted as ram pressure stripping of gas from infalling galaxies with vigorous star formation, transforming them from spirals to S0 or even elliptical galaxies.

LoCuSS (Local Cluster Substructure Survey) is studying a sample of nearby galaxy clusters with deep NIR and Spitzer photometry (Haines, Smith, Egami et al, 2010, arXiv:0908.3003). They find that using the near-IR light, which is less sensitive to star

formation, to determine the galaxy mass still leads to a Butcher-Oemler effect, in that the fraction of massive infrared luminous galaxies out of the total within r_{200} increases steadily with z for a sample of 27 clusters with $z < 0.3$. In particular, this excess arises from galaxies found at large cluster-centric radii between r_{500} and r_{200}. They suggest that the B-O effect can be explained by combining the global decline in star-formation in the universe since $z = 1$ with enhanced star formation in the infall regions of clusters at intermediate redshifts.

THE DEPENDENCE OF GALAXY COLORS ON LUMINOSITY AND ENVIRONMENT AT $Z \sim 0.4$[1]

H.K.C. Yee[2], B.C. Hsieh[3,4], H. Lin[5], M.D. Gladders[6]

ABSTRACT

We analyse the $B - R_c$ colors of galaxies as functions of luminosity and local galaxy density using a large photometric redshift catalog based on the Red-Sequence Cluster Survey. We select two samples of galaxies with a magnitude limit of $M_{R_c} < -18.5$ and redshift ranges of $0.2 \leq z < 0.4$ and $0.4 \leq z < 0.6$ containing $\sim 10^5$ galaxies each. We model the color distributions of subsamples of galaxies and derive the red galaxy fraction and peak colors of red and blue galaxies as functions of galaxy luminosity and environment. The evolution of these relationships over the redshift range of $z\sim0.5$ to $z\sim0.05$ is analysed in combination with published results from the Sloan Digital Sky Survey. We find that there is a strong evolution in the restframe peak color of bright blue galaxies in that they become redder with decreasing redshift, while the colors of faint blue galaxies remain approximately constant. This effect supports the "downsizing" scenario of star formation in galaxies. While the general dependence of the galaxy color distributions on the environment is small, we find that the change of red galaxy fraction with epoch is a function of the local galaxy density, suggesting that the downsizing effect may operate with different timescales in regions of different galaxy densities.

Subject headings: Galaxies: evolution — galaxies: fundamental parameters

Fig. 39.— Abstract of Yee, Hsieh, Lin & Gladders, ApJ, 2006

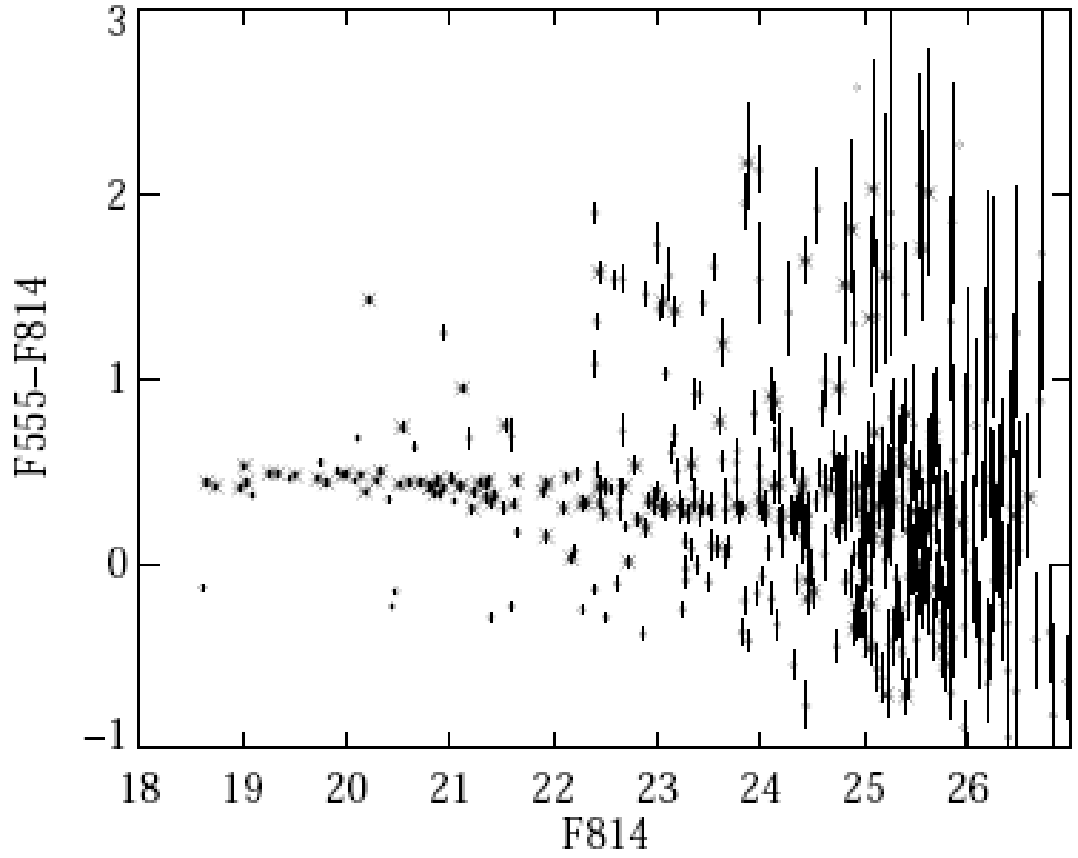

Fig. 1.— The observed color-magnitude diagram for Abell 2390, based on two-filter HST imaging of the cluster core. The data are from Gladders et al. (1998). The asterisks indicate galaxies morphologically selected as early-types, and diamonds indicate other galaxies in the image. Error bars are 1-sigma.

Fig. 40.— Fig. 1 of Gladders & Yee, 2000, AJ, 120, 2148

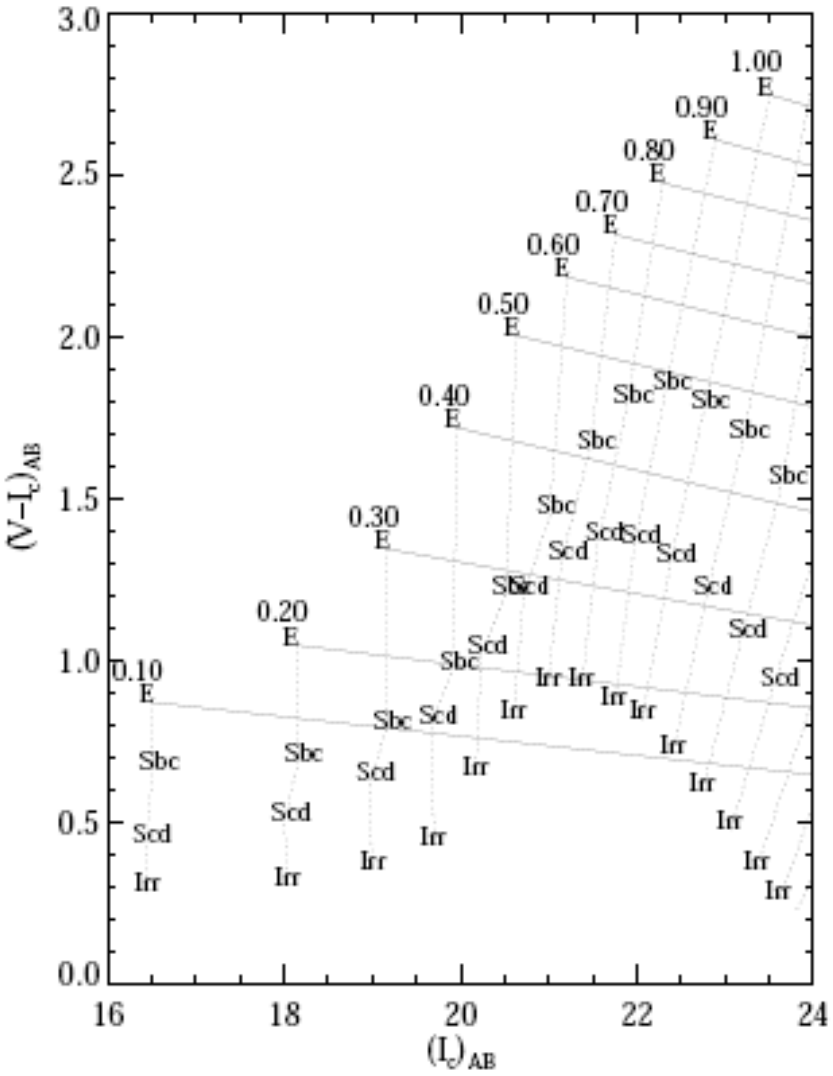

Fig. 2.— A simulated (V-I$_c$)$_{AB}$ vs. (I$_c$)$_{AB}$ color-magnitude diagram. Model apparent magnitudes and colors at various redshifts for several types of galaxies at a fixed M_I of -22. The dotted lines connect galaxies at the same redshift. Solid near-horizontal lines show the expected slope of the red sequence at each redshift.

Fig. 41.— Fig. 2 of Gladders & Yee, 2000, AJ, 120, 2148

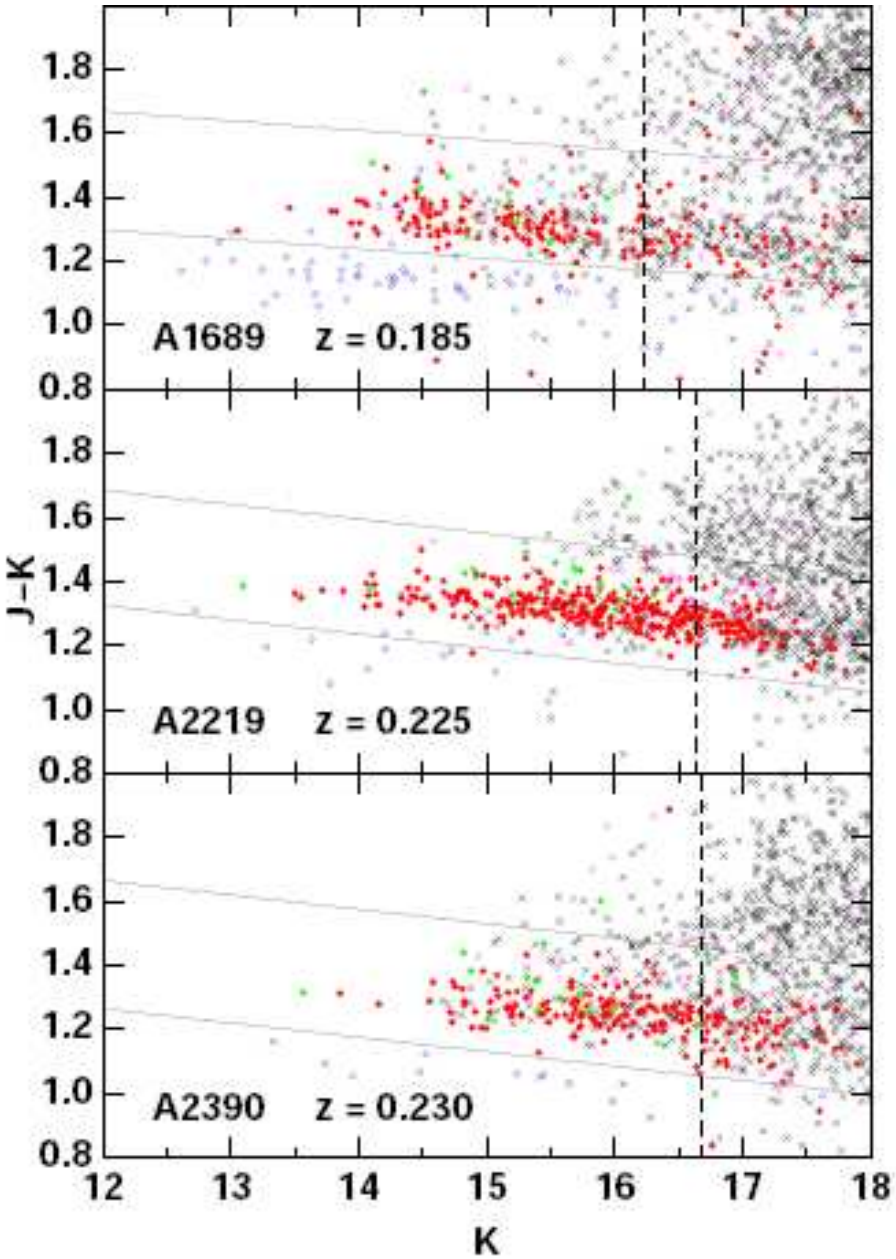

FIG. 1.— $J-K/K$ color-magnitude diagrams for galaxies within $1.5r_{500}$ of clusters A1689, A2219 and A2390. These three clusters are shown because their spectroscopic redshift catalogs are the most complete among the 22 clusters from LoCuSS. Filled symbols indicate spectroscopically-confirmed cluster members, with green (red) colors indicating those (not) having $L_{IR}>5\times10^{10}L_{\odot}$ based on their 24μm fluxes. Blue and magenta open symbols indicate foreground and background galaxies with redshifts respectively, while crosses indicate those galaxies without redshift information. The pair of sloping lines indicate the upper and lower boundaries of the color-magnitude selection used to identify probable cluster members. The dashed line indicates our faint magnitude limit of $K^*+1.5$.

Fig. 42.— Fig. 1 of Haines, Smith, Egami et al, 2010. LoCuSS cluster survey

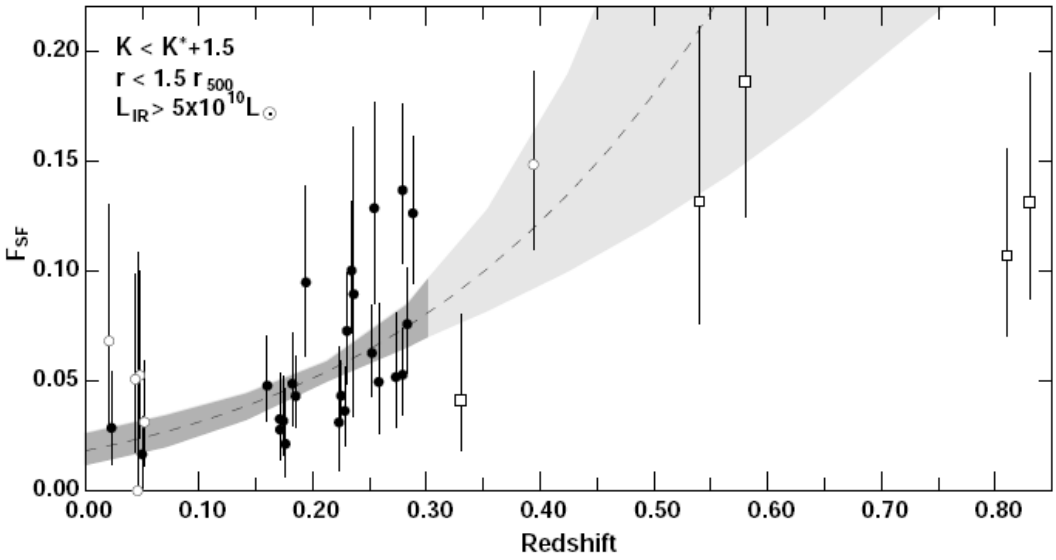

FIG. 2.— The mid-infrared Butcher-Oemler effect. The estimated fraction of $M_K \leq M_K^*+1.5$ cluster members within $1.5r_{500}$ having $L_{IR}>5\times10^{10}L_\odot$. The dashed line indicates the best-fitting evolutionary fit of the form $f_{SF}=f_0(1+z)^n$ to the $z<0.3$ clusters, and the shaded region indicates the 1σ confidence region to the fit, with the lighter colors showing the extrapolation of the fit beyond $z=0.3$. Solid circles indicate clusters with $L_X>3\times10^{44}\mathrm{erg\,s^{-1}}$, while open circles indicate less X-ray luminous clusters. The open squares indicate the values of f_{SF} taken from the Saintonge et al. (2008) $z>0.3$ sample.

Fig. 43.— Fig. 2 of Haines, Smith, Egami et al, 2010. LoCuSS cluster survey illustrating the Butcher-Oemler effect as seen in the near-IR.

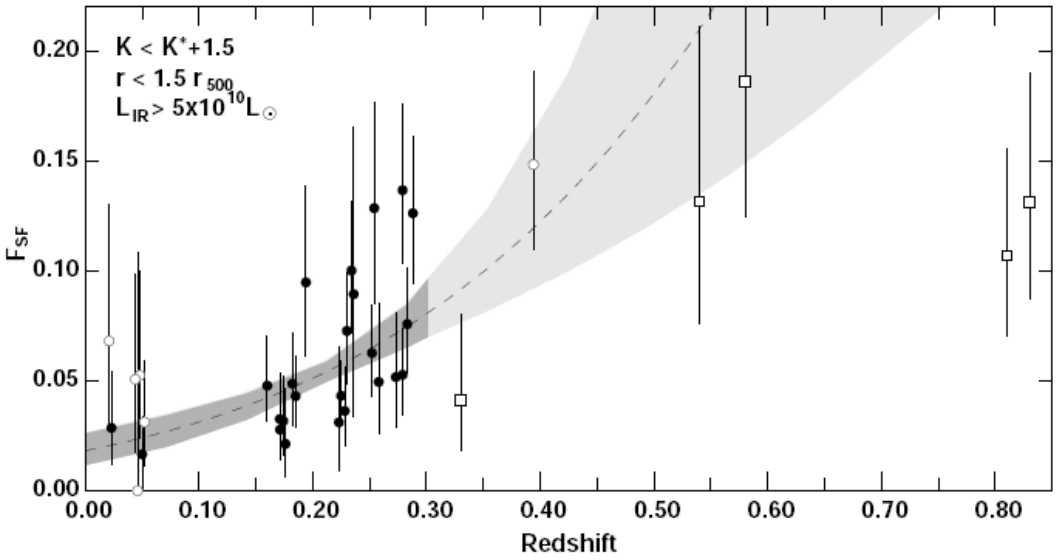

FIG. 2.— The mid-infrared Butcher-Oemler effect. The estimated fraction of $M_K \leq M_K^*+1.5$ cluster members within $1.5r_{500}$ having $L_{IR}>5\times10^{10}L_\odot$. The dashed line indicates the best-fitting evolutionary fit of the form $f_{SF}=f_0(1+z)^\alpha$ to the $z<0.3$ clusters, and the shaded region indicates the 1σ confidence region to the fit, with the lighter colors showing the extrapolation of the fit beyond $z=0.3$. Solid circles indicate clusters with $L_X>3\times10^{44}$ergs^{-1}, while open circles indicate less X-ray luminous clusters. The open squares indicate the values of f_{SF} taken from the Saintonge et al. (2008) $z>0.3$ sample.

Fig. 44.— Fig. 3 of Haines, Smith, Egami et al, 2010. LoCuSS cluster survey illustrating the spatial dependence of star-forming galaxies.

THE DEPENDENCE OF GALAXY COLORS ON LUMINOSITY AND ENVIRONMENT AT $Z \sim 0.4$[1]

H.K.C. YEE[2], B.C. HSIEH[3,4], H. LIN[5], M.D. GLADDERS[6]

ABSTRACT

We analyse the $B-R_c$ colors of galaxies as functions of luminosity and local galaxy density using a large photometric redshift catalog based on the Red-Sequence Cluster Survey. We select two samples of galaxies with a magnitude limit of $M_{R_c} < -18.5$ and redshift ranges of $0.2 \leq z < 0.4$ and $0.4 \leq z < 0.6$ containing $\sim 10^5$ galaxies each. We model the color distributions of subsamples of galaxies and derive the red galaxy fraction and peak colors of red and blue galaxies as functions of galaxy luminosity and environment. The evolution of these relationships over the redshift range of $z\sim0.5$ to $z\sim0.05$ is analysed in combination with published results from the Sloan Digital Sky Survey. We find that there is a strong evolution in the restframe peak color of bright blue galaxies in that they become redder with decreasing redshift, while the colors of faint blue galaxies remain approximately constant. This effect supports the "downsizing" scenario of star formation in galaxies. While the general dependence of the galaxy color distributions on the environment is small, we find that the change of red galaxy fraction with epoch is a function of the local galaxy density, suggesting that the downsizing effect may operate with different timescales in regions of different galaxy densities.

Subject headings: Galaxies: evolution — galaxies: fundamental parameters

Fig. 45.— Abstract of Yee, Hsieh, Lin & Gladders, ApJ, 2006

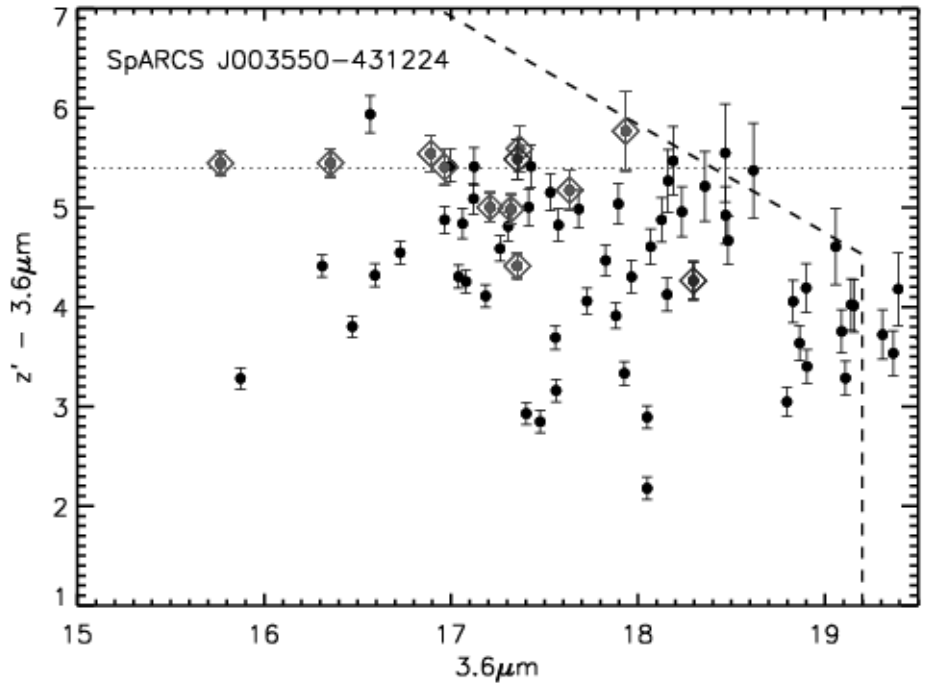

FIG. 6.— z'-[3.6] versus [3.6] color-magnitude diagram for SpARCS J003550-431224. The black circles are all the galaxies contained within a circle of radius 550 kpc (65″) at the cluster redshift. The red diamonds show the ten spectroscopically confirmed cluster members. The blue diamonds show the two (of the five) confirmed foreground/background galaxies which fall within the 550 kpc radius. The dotted line indicates the nominal red-sequence color for this cluster ($z' - [3.6] = 5.4$). See § 5 for a discussion.

Fig. 46.— Fig. 6 of Wilson, Muzzin, Yee et al (ApJ,2009). (z=1.34 gal cluster).

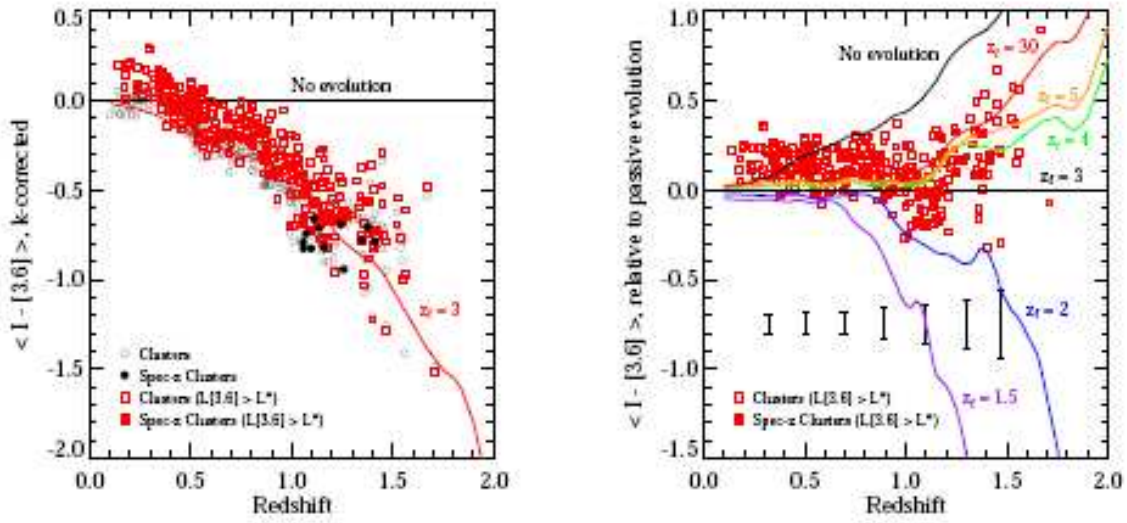

Figure 2. *(left)*: Mean, k-corrected I-[3.6] color vs. redshift for clusters in the ISCS (circles; filled symbols are confirmed $z > 1$ clusters). The red curve is a passively evolving $z_f = 3$ model. Red boxes are the mean colors of massive ($L > L^*$) galaxies only and are systematically redder than the overall cluster population. *right*: Mean I-[3.6] color relative to the $z_f = 3$ PE model. Clusters at $z \gtrsim 1.2$ formed their stars at very high redshift ($z_f \gtrsim 4$).

Fig. 47.— Fig. 2 of Brodwin, Eisenhardt, Gonzalez et al, 2009.

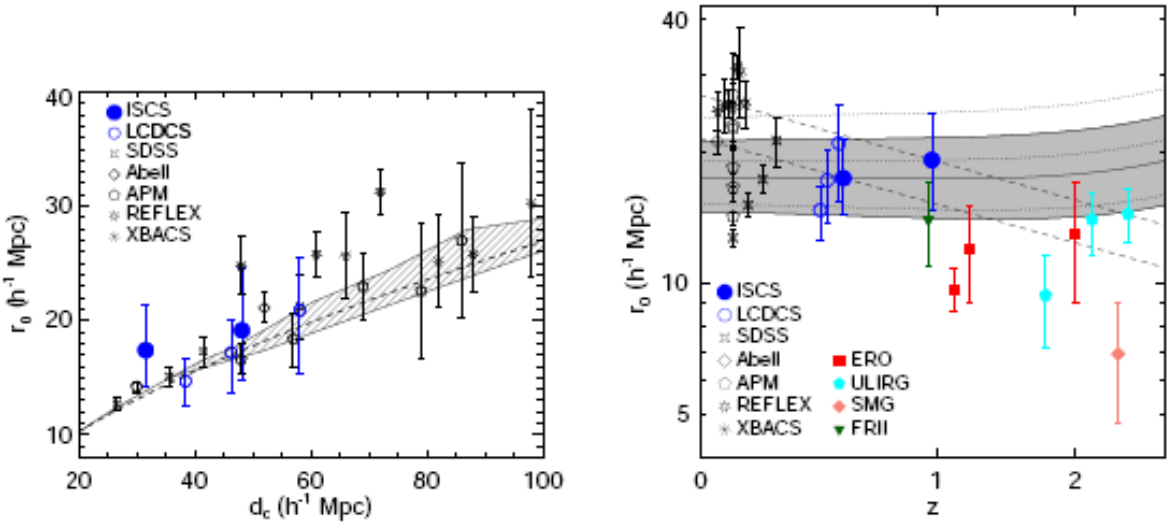

Figure 3. *Left*: r_0 vs. d_c for the present sample (filled circles) along with several $z \lesssim 0.5$ measurements from the literature (Bahcall et al. 2003, and references therein). The hashed region shows the ΛCDM prediction over $0 < z < 1.5$ (Younger et al. 2005). *Right*: Comoving correlation lengths for the ISCS clusters, other cluster samples at low-z, and high-z, highly clustered galaxy populations. The filled region (dotted lines) illustrates the predicted r_0 evolution in a biased structure formation model for our $z_{\rm eff} = 0.53$ (0.97) cluster samples. The dashed lines represent simple stable clustering models.

Fig. 48.— Fig. 3 of Brodwin, Eisenhardt, Gonzalez et al, 2009.

1.8. Relevant Theory

Dave & Oppenheimer, (2007, MNRAS, 374, 427) use cosmological simulations to model the enrichment history of baryons in the Universe, "metals" (i.e. C or O) traced for z from 6 to 1.

Oppenheimer, Dave, Keres et al (2010, MNRAS, in press, see arXiv:0912.0519) include feedback and recycled wind accretion: assembling the z=0 galaxy mass function Considers fate of SNII ejecta that escape from a galaxy - does it fall back, get pushed far out into the halo but remain bound, or escape into the IGM ?

1.9. The IGM as Revealed By QSO Absorption Lines

Lecture to be given by W.L.W. Sargent. Major issues include ionization field and formation of dust which depletes elements in the gaseous phase onto dust grains.

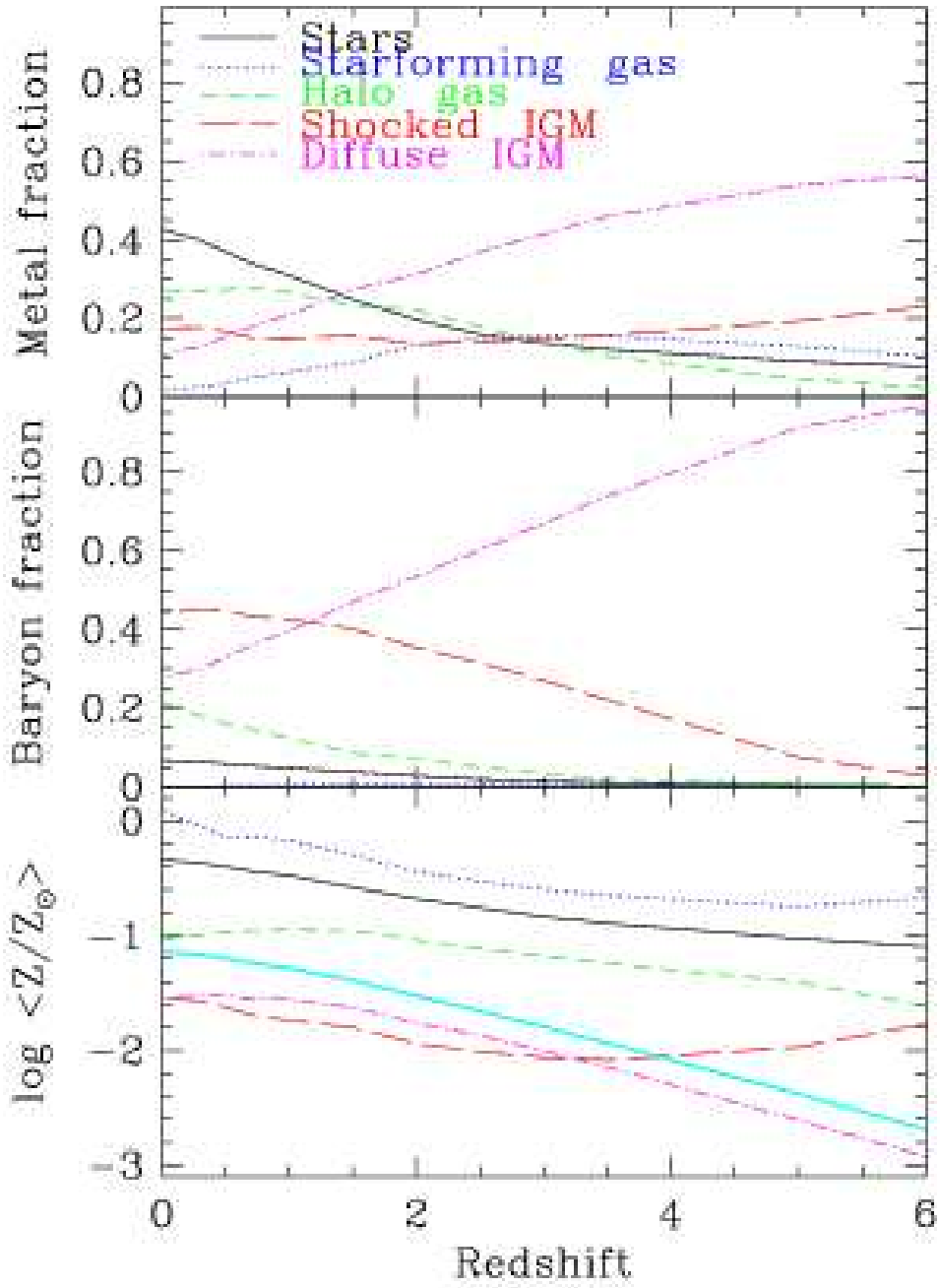

Figure 1. *Top:* Metal mass fraction in various baryonic phases as a function of redshift: Stars (black solid), star-forming gas (blue dotted), halo gas (green dashed), shocked IGM ($T > 10^{4.5} K$; red long-dashed), and diffuse IGM (cyan dot-dashed). *Middle:* As above, for total mass fraction of baryons. *Bottom:* As above, for metallicity. The thick cyan line represents the mean mass-weighted metallicity of the universe.

Fig. 49.— Fig. 1 of Dave & Oppenheimer, 2007

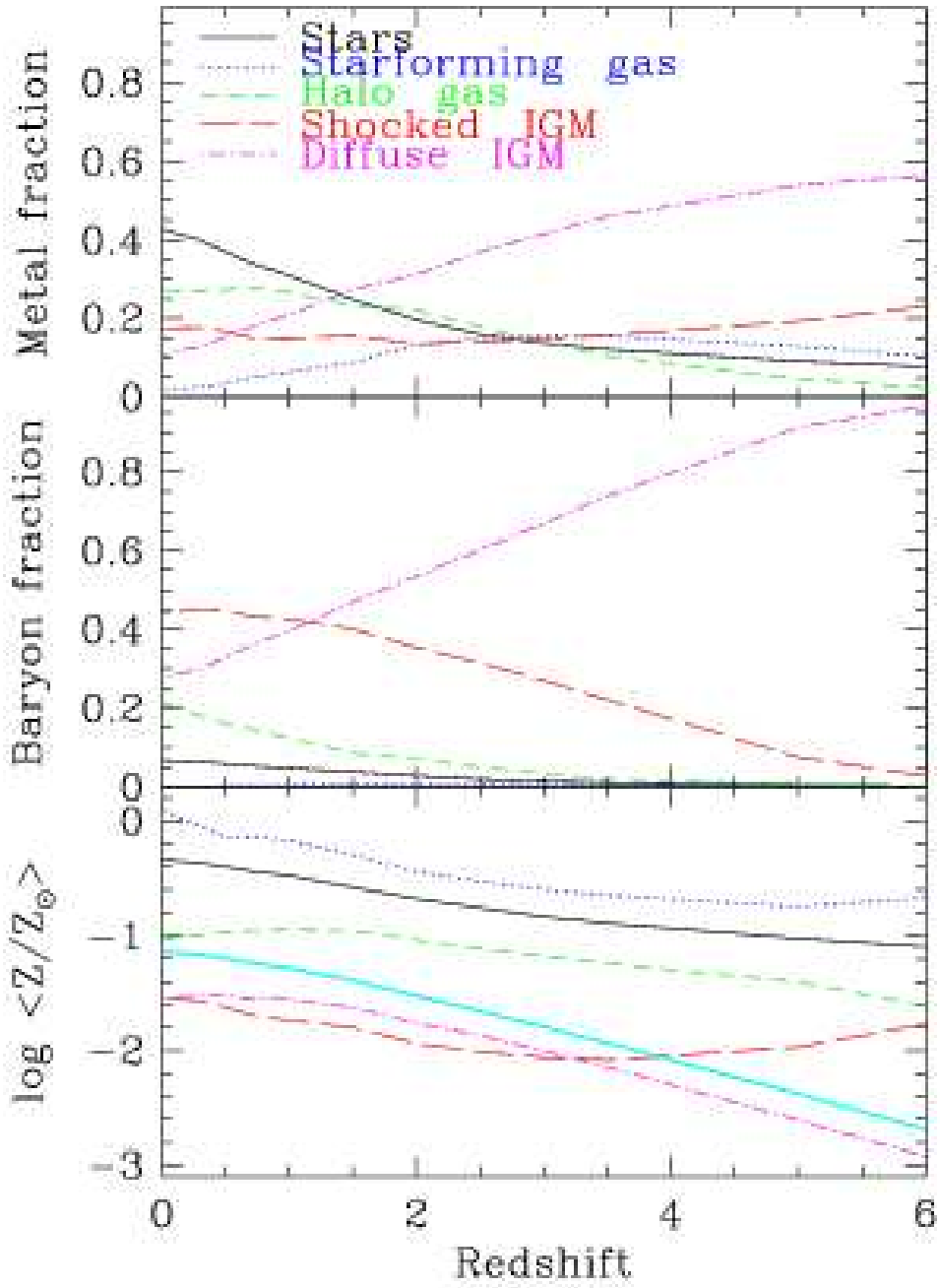

Figure 1. *Top:* Metal mass fraction in various baryonic phases as a function of redshift: Stars (black solid), star-forming gas (blue dotted), halo gas (green dashed), shocked IGM ($T > 10^{4.5} K$; red long-dashed), and diffuse IGM (cyan dot-dashed). *Middle:* As above, for total mass fraction of baryons. *Bottom:* As above, for metallicity. The thick cyan line represents the mean mass-weighted metallicity of the universe.

Fig. 50.— Fig. 3 of Dave & Oppenheimer, 2007

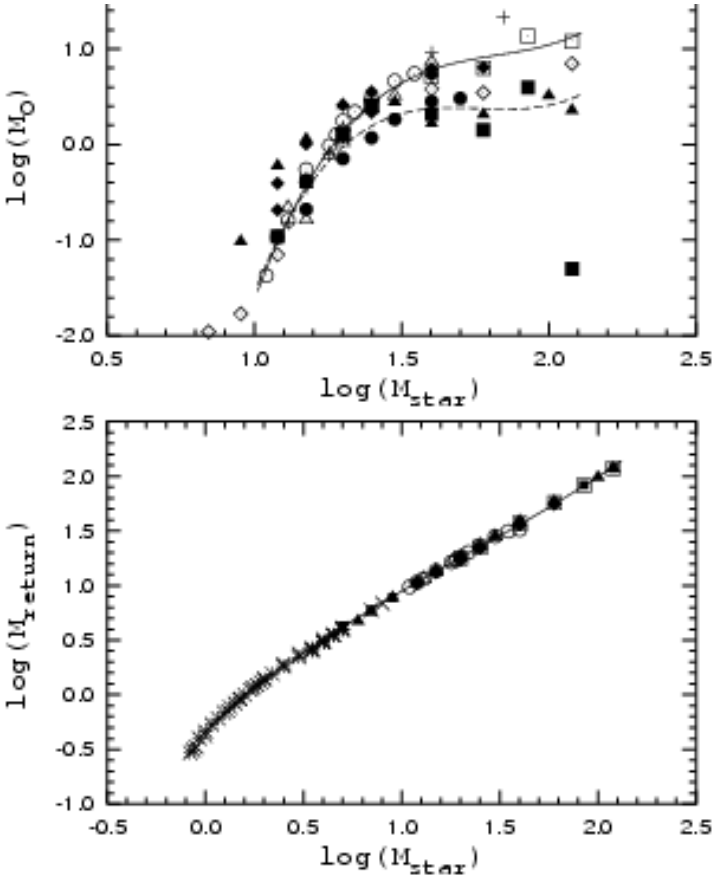

Figure 4. *Top panel.* The mass of freshly manufactured oxygen ejected by a star in the interstellar medium as a function of the initial mass of the star. The results from Maeder (1992) for models with low stellar wind mass loss rates are shown by open squares, and that for models with high stellar wind mass loss rates are shown by filled squares. Results from other investigators have also been plotted: Langer & Henkel (1995) (filled circles), Nomoto et al. (1997) (plus signs), Portinari et al. (1998) (filled triangles), Meynet & Maeder (2002) (open rhombus), Hirschi et al. (2005) (filled rhombus), and Kobayashi et al. (2006) (open triangles). The solid line is a fit to the model results of Maeder (1992) (models with low stellar wind mass loss rates), Woosley & Weaver (1995), Nomoto et al. (1997), and Kobayashi et al. (2006). The dashed line is a fit to the model results of Maeder (1992) (models with high stellar wind mass loss rates), Langer & Henkel (1995) and Portinari et al. (1998). *Bottom panel.* The mass returned by a star to the interstellar medium as a function of the initial mass of the star. The data for low- and intermediate-mass stars from van den Hoek & Groenewegen (1997) are shown by crosses, those from Marigo (2001) by open circles. The sources for the models and the symbols for massive stars are the same as in the top panel. The solid line is a fit to all the data.

Fig. 51.— Fig. 4 of Pilyugin, Thuan & Vilchez, (2007, MNRAS, 376, 353). ***This figure needs to be moved to an earlier lecture.***

Suggested Reading:

Kewley & Ellison, 2008, ApJ, 681, 1183 Metallicity Calibrations and the Mass-Metallicity Relation for Star-Forming Galaxies (calibration of Mass-metallicity relation and application to star-forming galaxies $z < 0.1$ in SDSS.

Kewley, Groves, Kauffman, Heckman, 2006, MNRAS, 372, 961 The Host Galaxies and Classification of AGN

Pilyugin & Thuan, 2007, ApJ, 669, 299 O Abundance of Nearby Galaxies from SDSS spectra

Pilyugin, Thuan & Vilchez, 2007, MNRAS, 376, 353. On the Maximum value of the cosmic O abundance and the O yield

Tremonti, Heckman, Kauffmann et al, 2004, ApJ, 613, 898 The Origin of the mass-metallicity relation: insights from 53,000 star-forming galaxies in the SDSS.

Kauffmann, Heckman & White et al, 2003m, MNRAS, 341, 33 Stellar masses and star formation histories for 10^5 galaxies from the SDSS

C. Leitherer - Spectral Evolution Models for the Next Decade, 2010, in *Stellar Populations – Planning for the Next Decade*, arXiv:0910.1327

D. Osterbrock, classic book, *Astrophysics of Gaseous Nebulae and Active Galactic Nuclei*

D. Erb - Chemical Abundances in Star-Forming Galaxies at High Redshift, for IAU Symposium 265, 2009, *Chemical Abundances in the Universe: Connecting First Stars to Planets*

Erb, Shapley, Pettini, Steidel, Reddy & Adelberger, 2006, ApJ, 644 813, The Mass-Metallicity Relation at $z \sim 2$